# MODELING AND TESTING OF A MILLIWATT HYDROKINETIC TURBINE FOR PRESSURE ENERGY HARVESTING

By Heather P. Cantin

A Thesis

Submitted in Partial Fulfillment

of the Requirements for the Degree of

Master of Science

in Engineering

Northern Arizona University

May 2018

Approved:

Michael W. Shafer, Ph.D., Chair

Tom Acker, Ph.D.

Peter Vadasz, Ph.D.

# ABSTRACT

## MODELING AND TESTING OF A MILLIWATT HYDROKINETIC TURBINE FOR PRESSURE ENERGY HARVESTING

HEATHER P. CANTIN

Technologies such as telemetry and remote sensing systems are commonly used to gain information that is not easily obtainable by the researcher. The challenge, however, is that these systems do not have access to an external power supply once deployed in a desolate location. This limits their lifespan to the energy density of an on-board battery and creates a constraint on their sensing capabilities and data resolution. Often times the batteries are not rechargeable and need to be replaced, which is especially difficult and costly for marine telemetry systems, as they are typically encased in epoxy resin to withstand high pressures at depth. Such systems would benefit greatly from energy harvesting. In the marine environment, the great pressures that are experienced at depth provide a vast amount of potential energy that can be harvested. Marine animals equipped with telemetry tags are the perfect candidates as many species make frequent dives while foraging or migrating. This energy can be converted to mechanical and electrical energy with the use of a turbine, which is commonly used for small to large-scale energy production. However, turbines on the scale needed for this application is not readily available. There has been an increase in the research of millimeter-scale turbines for small power generation, but they are usually air or gas powered and few provide an in-depth analysis of the efficiencies of these sys-

tems. This thesis focuses on the development and testing of a millimeter-scale hydrokinetic turbine for harvesting energy for marine telemetry tags and like-systems. An analytical model is developed using common turbomachinery concepts and compared to experimental results of a turbine prototype to identify and quantify sources of loss. Each identified loss is thoroughly explained as it is applied to the model and suggested design improvements are discussed. The model is used to make predictions of turbine performance given a higher input pressure for assessment of the viability of this transduction method for the intended application. The model and design presented provides useful information for future exploration of miniature turbine technology for powering remote micro-systems and insight into pressure energy harvesting capabilities.

# Acknowledgements

First and foremost, I would like to thank my advisor Dr. Michael Shafer for his continuous support and inspiring enthusiasm. This thesis could not have been accomplished without his involvement in this work and dedication to my success as a student and researcher. I am forever grateful for the knowledge you have shared and the skills I have gained as your student.

I would also like to show appreciation to my advisory committee, Dr. Tom Acker and Dr. Peter Vadasz, for taking the time to review this thesis and provide feedback. I have also enjoyed attending many of your classes and I am thankful for all that I have learned from you throughout the years.

Thank you to my family and friends for their love, encouragement, and understanding throughout all stages of my schooling. I am fortunate to have you cheering me on to the finish line each and every time.

Most importantly, I dedicate this work to my husband for his selfless love, patience, and support throughout the best days and the sleepless nights. No words can express my gratitude for you and all you have done to ensure I reach my goals.

# Contents

# List of Tables

# List of Figures

# Chapter 1

# Introduction

## 1.1 Motivation

Telemetry and remote sensing systems are used extensively by scientists to gain information about wildlife and the environment within and beyond the Earth's atmosphere. The technologies used to collect this information typically reside in desolate locations making it challenging to obtain access to additional power when needed. Although improvements are continuously being made to battery chemistry to increase energy density, their lifespan ultimately creates a limit on the system's deployment time and data resolution [8, 9, 10]. Systems affected by this constraint would benefit greatly from the development and implementation of energy harvesting methods to supplement or replace the current power source.

Energy harvesting utilizes an ambient source to convert into useful electrical power [11]. Energy harvesting research for self-powered devices has grown tremendously over the last couple decades, as it is an attractive capability for a wide variety of micro-systems. Some of the most commonly available sources for energy harvesting

include: motion/vibration, electromagnetic, thermal, pressure gradients, fluid flow, and solar/light. Harvesting of these sources has been demonstrated on a variety of products, from biomedical applications, to railway tracks, to wildlife monitoring devices [12, 13, 14].

Wildlife monitoring is a good example of a technology that is highly affected by the limitations of their current power source, as the implentation of harvesting technologies is currently sparse. Increasing the deployment time of these systems would allow for increased data collection over multiple seasons or even years as the animal matures [15]. This is important for studying the ever-changing and evolving migration patterns of wildlife and the state of the surrounding environment over time. The increased longevity of the technology also decreases the amount of human interaction with the wildlife, enhancing the safety of the researcher and well-being of the animal. The limitation of system lifespans is a result of the on-board batteries, which also contribute greatly to the weight, size, and maintenance or replacement costs. Fortunately, there is an abundance of harvesting opportunities animals provide from their behavior, body chemistry, and environment.

The marine biology community, specifically, has expressed their need for alternative methods of obtaining power for their remote systems and tags [16]. A collaboration with the Costa Lab at the University of California, Santa Cruz has sparked the initial research of potential energy harvesting methods for marine wildlife telemetry systems with the Dynamic and Active Systems Lab (DASL) at Northern Arizona University. The main focus of this collaboration has been narrowed down to solar energy, hydrostatic pressure fluctuations, and fluid flow related to animal motion, as all are predicted to be viable energy sources for specific species. One of the species the Costa

Figure 1.1: A marine telemetry tag mounted on a Northern Elephant Seal. Photo by Dan Costa [2].

Lab studies extensively is the Northern Elephant Seal (*Mirounga angustirostris*) and an example of a telemetry tag attached to this species is shown in Figure 1.1.

The focus of this research is the harvesting of energy from hydrostatic pressure fluctuations, inspired by the frequent diving behavior of various pinnipeds, sea turtles, and cetaceans. The method of harvesting explored includes an internal, hydrokinetic turbine derived from turbomachinery and hydropower concepts. However, the proposed system size presents challenges for identifying and quantifying losses that may be experienced that ultimately affect the efficiency. The focus of this work is on the initial development of a small and scalable turbine prototype and assessment of the system's mechanical power output and efficiency for a given input fluid pressure using an analytical model. The evolution of the model as losses in the system are identified is discussed in depth along with the methods used to quantify them. Once the model results are verified with the experimental data, predictions are made for a higher input pressure to assess the viability of this system for small power generation. It is important to note that while the application used in this paper is specific to marine animals, the work presented here is not limited to that application alone. With the

growth of technology in ocean exploration comes more opportunities for advancement of their capabilities and longevity. Systems that may also benefit from pressure energy harvesting include submersibles, such as autonomous underwater vehicles (AUV) and remotely operated vehicles (ROV), and diver equipment. Furthermore, any system which maintains a constant fluid pressure difference could deploy an energy harvester similar to that presented here. While this work does not present a complete assembly for implementation and instead focuses on the mechanical energy conversion, the desired future work and applications for this system is discussed.

## 1.2 Aim of research

The aim of this research is to provide a mathematical interpretation of a hydrokynetic turbine design and explore the potential of using this technology to power small marine telemetry and applicable submerged systems with a pressure-differential source. The contribution of this work combines and modifies the known analysis methods of common turbomachinery and hydropower systems to adequately model a turbine prototype on the scale of millimeters. The verification of the analytical model through experimental testing provides identification and quantification of losses experienced on this scale. The effects of downsizing on efficiency due to these losses will provide information for future exploration and implementation of miniature turbine technology for remote micro-systems.

## 1.3 Thesis outline

### 1.3.1 Chapter 2

In this chapter, literature and additional sourced information pertaining to this research is presented. The chapter begins with a discussion of the various features and energy expenditure of common marine telemetry tags, followed by current energy harvesting methods implemented on tags across all wildlife. Notable literature highlighting pressure energy harvesting methods and applications is also discussed in depth. Lastly, published microturbine technology inspiring to this research is discussed, including design, experimental results, and loss analysis.

### 1.3.2 Chapter 3

The purpose of this chapter is to define the turbine design concept to be used to transfer pressure energy into harvestable energy. Specifically, the stator and rotor relationship of the system is defined and expressed in graphical form. The mathematical relationship between key characteristics and velocity components combined with the momentum equation to determine torque, power output, and mechanical efficiency is presented. This chapter provides the base of the analytical model.

### 1.3.3 Chapter 4

This chapter encompasses all contributions to experimental testing of the turbine. The experimental setup configured for prototype testing is defined. Evolution of the stator and rotor prototypes is expanded to include losses identified early in the development stages and how these losses were reduced for future designs. Lastly, the

experimental test results of the final optimized prototype are presented, analyzed, and discussed.

### 1.3.4 Chapter 5

In this chapter, the analytical model is compared to the experimental results and modified to increase its accuracy in predicting turbine performance. Losses in the system are further explored and quantified. An in-depth discussion of the methods and tools used to evaluate each loss is presented, followed by a discussion of any remaining uncertainties.

### 1.3.5 Chapter 6

The purpose of this chapter is to apply the analytical model to predict the turbine's performance for an intended application. The prediction includes a higher pressure input than what is tested experimentally. Then the turbine output is theoretically matched to an off-the-shelf motor/generator to determine the electrical power out efficiency of the system. The performance results and power provided by the system is then compared to the energy extracted from the application's current energy source. Lastly, a discussion of how the turbine may be integrated into an intended application is addressed.

## Chapter 2

# Literature Review

In order to assess the viability of an energy harvesting method capable of powering telemetry and remote sensing systems, it is important to complete a review of existing technologies and understand the tools needed for development of a design. This chapter includes a collection of information pertaining to pressure energy harvesting and turbine technology, in addition to a brief look at state-of-the-art energy harvesting technologies and energy assessment of a potential application.

## 2.1 Marine bio-logging technology

As the focus of this research is the application of energy harvesting for telemetry systems in the marine environment, it is important to acknowledge the energy expenditure of such systems. The example application here has been narrowed to marine animal telemtry systems, also known as biologgers, as per request of the biology research community. The three main types of marine biologgers used in the field today, include recorder tags, position-only tags, and position-and-data tags. Recorder tags

store the data on-board and therefore, the information can only be retrieved by the researcher once detached from the animal. These tags consume up to 80 J of energy per day and have a maximum deployment time of five years [17, 18, 19]. Position-only tags utilize systems such as the Advanced Research and Global Observation Satellite (ARGOS) network to determine location and/or upload GPS coordinates for the researcher to view while the tag is still deployed. However, there is a limit to the amount of sensor data that can be transmitted. The position-only tags consume up to 150 J of energy per day and have a maximum deployment time of 3.5 years [19]. Lastly, position-and-data tags are of the highest grade of marine biologgers. They utilize the ARGOS network to provide position information and transmit the data acquired by the tag, which can include temperature, depth, salinity, etc. While they offer the ideal system for data collecting, position-and-data tags can consume around 300 J of energy per day for a maximum deployment time of about one year [19, 20, 4]. A plot of the computed daily energy consumption and tag lifetimes can be seen in Figure 2.1.

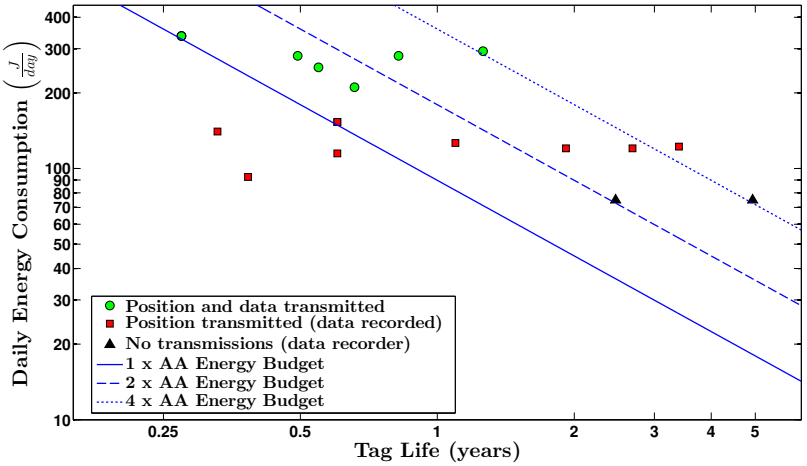


Figure 2.1: Daily energy budget for a wide range of marine biologgers [3]. Energy estimates are based on Wildlife Computers™ tags.

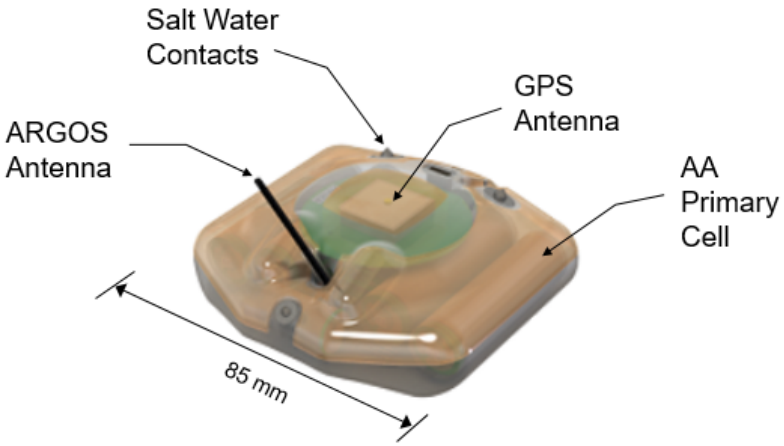


Figure 2.2: A Wildlife Computers™ SPLASH10-F-296 pinniped tag, which utilizes Fastloc and ARGOS tracking, equipped with depth, temperature, and light sensors [4].

The objective of integrating an energy harvesting method would be to increase tag lifetimes, while maintaining the technologies and data collecting capabilities that is desired by researchers. This would also decrease tag replacement costs for the biologists, as the batteries, encased in epoxy-resin, are not easily replaced [21]. An example of a bio-logger commonly used in the field for pinnipeds and sea turtles is shown in Figure 2.2. The enclosed AA battery is typical of those used in many marine telemetry tags. The most common cell used by Wildlife Computers™ is a Li-$SOCL_2$ battery with an energy density of 4.03 kJ/$cm^3$ [19].

## 2.2 Energy harvesting for environment and wildlife monitoring systems

The application of energy harvesting has grown tremendously with advancements in low-power technology and wireless network sensors, while batteries continue to fall

short due to their limited capacity [22]. Common sources for harvesting include, but are not limited to, vibration or displacement, thermal, electromagnetic, solar, pressure gradients, and fluid flow [11]. Research and development of vibration energy harvesting by piezoelectrics has been demonstrated on small telemetry tags for flying insects and birds [23, 15, 14]. However, specific to environment and wildlife monitoring, solar power by photovoltaic cells is the most common utilized source in the field. Although still limited, marine, land, and avian species, have been fitted with solar powered telemetry in the form of various tags and collars [24, 25, 26]. Autonomous Underwater Vehicles (AUV), which are unmanned underwater vehicles used for a variety of marine applications, have also been equipped with photovoltaic cells in some cases [27]. An additional harvesting method has been explored for AUVs in which the propulsion is powered by the ocean temperature variation at depth causing a phase change in a working fluid [28, 29]. Pressure energy harvesting for remote marine applications has been explored in previous work as well, which will be discussed in the following section. Although a number of methods have been explored or are currently utilized in the field, the implementations are still minimal and it is important to continue to explore novel ideas, such as pressure energy harvesting, for applications where other methods may not be viable, particularly in the marine environment.

## 2.3 Pressure energy harvesting

The vast change in pressure that is available from varying ocean depth provides the potential for viable energy harvesting. Marine animals present this change in pressure as many species make frequent dives throughout the day to forage for food during migration, search for a mate, or obtain oxygen as needed. An example of the vast

changes in pressure that biologgers see is shown in the diving profile of a Northern elephant seal (*Mirounga angustirostris*) in Figure 2.3 [5]. At a depth of 60 meters, the seal experiences approximately 6.95 atm (102 psia) of total pressure. This data was derived from the first day of a migration, in which the seal was moving away from shore, limiting the dive depth to the ocean floor. At sea, Northern elephant seals typically reach much more extreme depths, routinely about 600 meters, but have been seen as deep as 1600 meters [30]. The frequency of this deep diving behavior also demonstrates how many pressure-cycles could be harvested within one day if the harvesting device is equipped to do so. Figure 2.3 presents an estimated 65 dive cycles in one day. Shafer et. al. presented a rough estimate of the energy that could potentially be harvested during the dive patterns of various marine species [31]. The estimates were based on pressure at a given ocean depth as a measure of energy per unit volume, or $p = \rho gh$, a calculation independent of a transduction method. The estimated energy was calculated using a sample volume of 250 $cm^3$, such that $E = pV$. For example, a Northern elephant seal reaching a depth of 428 m per dive, averaging 60 dives per day, could harvest 65 kJ/day with an input pressure of 43 atm. The required efficiency of the harvesting system would only need to be 0.31% in order to meet an energy target of 200 J/day. Even for more shallow divers, such as the Leatherback sea turtle (*Dermochelys coriacea*), an estimated efficiency of only 1.3% would be required for an average depth of 29 m at 10 dives per day. The low conversion efficiencies emphasize the large amount of pressure energy beneath the ocean's surface available for harvesting.

In 2007, Wang et. al. developed a pressure energy conversion system for providing power to an autonomous seafloor observatory [6]. The system, as shown in Figure

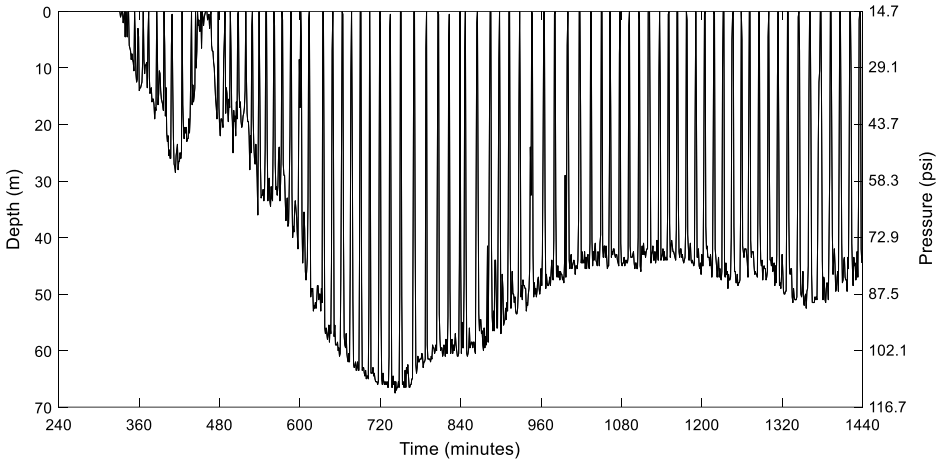


Figure 2.3: First 24 hours of migration of a Northern Elephant Seal showing depths and pressures reached below the ocean's surface. Data provided by The Costa Lab at the University of California, Santa Cruz [5]. Used with permission.

2.4, is placed on the sea floor at an extensive depth where high pressure exists. A 200 L elastic bladder filled with hydraulic oil is compressed under the seawater pressure at a controlled rate, driving the oil through a hydraulic motor coupled to an electric generator to an empty pressure chamber. At a depth of 2400 m, the system resulted in a conversion efficiency of 63.8% and produced 1180 W of electrical power. Once the pressure across the system equalizes, the system must be reset. However, to recharge the system, more power is needed than was generated to pump the hydraulic oil from the chamber back into the bladder. The system would need to be resurfaced for each recharge, which defeats the purpose of this stationary energy harvesting system. In reference to only the power generation stage, the power output of this system depends greatly on the size of the bladder and pressure chamber, which may present an issue for use on small telemetry systems. However, small systems also require less energy and are not stationary, increasing the potential to harvest additional energy rather

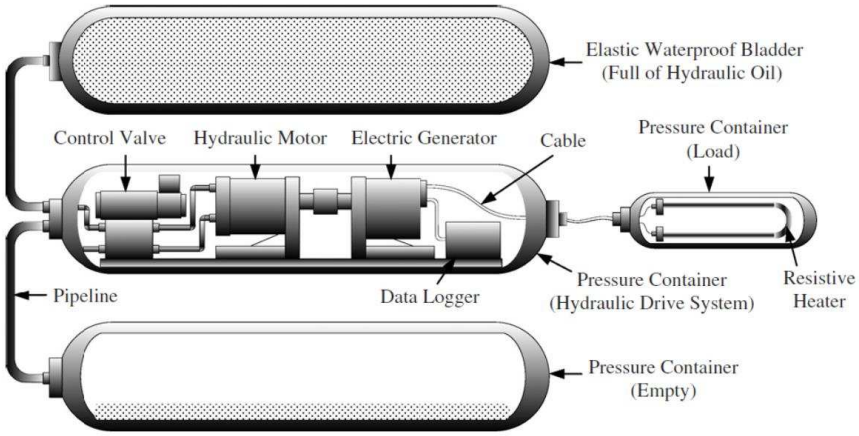


Figure 2.4: System structure of a pressure energy conversion device for powering an autonomous seafloor abservatory [6]. Used with permission.

than having to reset the system at the expense of the total power output.

Shafer et. al. explored the potential of a similar system for marine telemetry application [3]. The concept is that as the animal dives, a check valve opens to allow seawater to flow through a turbine, a micropump in reverse, into a flexible bladder within a gas-filled accumulator at ambient pressure until the fluid pressure equalizes across the system. During the ascent, the surrounding seawater pressure becomes less than the pressure within the accumulator, causing the now compressed gas to push the fluid within the bladder out through a second turbine into the surroundings to return to equilibrium once again. During the experimental validation, only the decent stage was tested and resulted in a maximum efficiency of 2.17% for an input pressure of 50 psi. It is predicted that the main diminishing factor of the system's efficiency is related to the use of the micropump for a purpose in which it is not optimally designed for. Optimizing a turbine specifically for this purpose suggests a drastic increase in system efficiency. However, there are no hydrokinetic turbines on the scale needed currently available on the market and the exploration of such a system's power and

conversion efficiency within the science community is minimal. Due to the potential that is still present in the overall pressure-energy harvesting systems presented above, a more efficient internal transduction method is deemed worth exploring for micro applications.

## 2.4 Microturbine technology

While there is minimal research available regarding hydrokinetic turbines for micro-systems, there have been multiple studies and development of pressurized air or gas-driven millimeter-scale turbines. Dental turbine handpieces, for example, have been used in industry for over 30 years and although they do not power an electrical system, they directly transfer pressurized air to fast rotational speeds of a drill tip, successfully, with an impulse turbine diameter of less than 5 mm [32]. These turbines are found to be approximately 24% efficient with an operating pressure of 2 bar [33]. Figure 2.5 displays one example of the internals of a dental handpiece head [7]. Within the energy harvesting realm, different styles of air/gas turbines have been explored, such as radial inflow, mixed inflow, variations of impulse designs, and axial flow. Radial inflow gas generators have seen efficiencies of 60% for turbine diameters of 6 mm and 10 mm with mass flow rates of 0.28 g/s and 1.53 g/s, respectfully [34, 35].

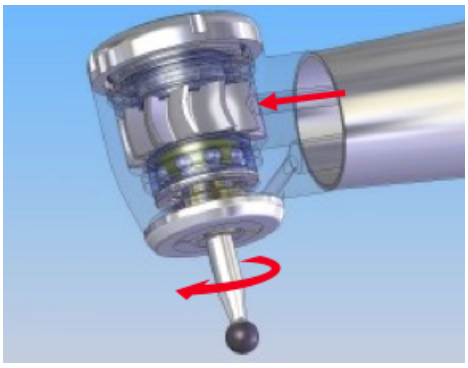

Figure 2.5: Internals of a dental handpiece head, including the direction of the pressurized air, the turbine rotor, and rotation of the drill tip [7].

An axial flow, impulse microturbine (Figure 2.6(a)), measuring only 10 mm in diameter, reached a mechanical efficiency of 18% and produced 28 W of mechanical power at 14.5 psi of compressed air [36]. The microturbine, designed and tested by Peirs et. al., was created to power small electronic devices and is intended to be run by fuel in future work. The author broke down the mechanical and electrical efficiencies into percentages of contributing causes for loss in the system and experimental setup. The flow chart of the losses can be seen in Figure 2.6(b). Unfortunately, an in-depth analysis of how these losses were quantified is not included in the discussion, yet the chart provides a good reference for what may be expected. This lack of in-depth analysis is perceived to be a common trend in literature pertaining to millimeter-scale turbine systems. However, many of these systems often include Computational Fluid Dynamics (CFD) modeling and analysis to compare with a prototype experiment. While this is a useful, and sometimes quick, tool for quantifying and locating losses, this does not help the reader understand the system mathematically if a modeling tool was not available.

(a)

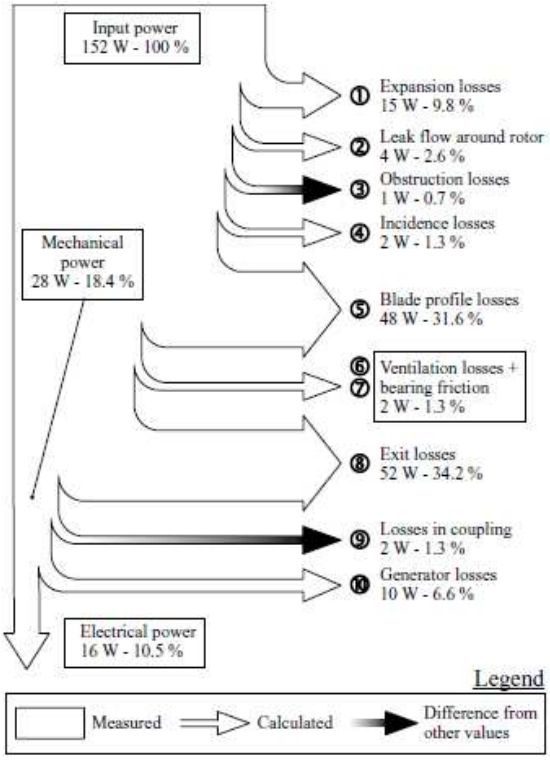


(b)

Figure 2.6: (a) Microturbine prototype, measuring 10 mm in diameter, tested for powering small electronics and (b) the associated losses identified in the system and experimental testing [36]. Used with permission.

## 2.5 Summary

This chapter presented applicable literature and technologies pertaining to the scope of this research. As the purpose of this research is driven by the support of the marine biology community, the current energy expenditure of commonly used marine telemetry tags was discussed. Optional applicable energy harvesting methods were presented through examples of technologies explored for or currently implemented into land, avian, and marine wildlife monitoring devices, which is fairly limited. The high potential of harvesting energy from static pressure and pressure fluctuations in the marine environment specifically was explored further with the discussion of current literature's pressure energy harvesting assessments and experiments. Lastly, the proposed transduction method of micro-turbine technology was explored, which briefly discussed a few of the available design types and their energy transfer or harvesting efficiencies. A considerable amount of experimental data is available for various configurations of turbines on this scale, yet more common for air or gas powered systems. However, the lack of analysis is noted and helps drive the motivation of this research to contribute further to this field.

## Chapter 3

# Design Concept and Modeling

The proposed turbine design and the desirable features it encompasses for application in marine telemetry systems is presented here. The design is first modeled graphically, then analytically from the derivation of known fluid dynamics and turbomachinery methods. The result is a clear understanding of key geometric features and their relationship with the fluid flow magnitude and direction and an equation for the torque on the turbine shaft that can be used to model mechanical power output and efficiency.

## 3.1 Design concept

The turbine design is inspired by the relationship between the stator and rotor rows of turbomachinery, as well as the current micro-scale turbine technology mentioned in previous sections. As the literature review presented, there are various types and flow configurations of turbines, such as axial, radial, and mixed flow. Depending on the type, a turbine can result in high rotational speeds with low torques or vice

versa. When choosing a turbine configuration, the end use of the turbine played a large role. For implementing a turbine in a harvesting system for a marine telemetry tag, the turbine would idealy be internal, sealed from the ocean environment, and constrained to an allowable system size. With these factors in mind, an axial flow turbine presented a feasible option due to the scalability, manufacturability, and shape of the system in relation to the current integrated batteries. A benefit of axial flow is the uniformity of the flow direction at the inlet and outlet of the turbine, as they are both parallel to the shaft or axis of rotation. An example of axial flow is shown in Figure 3.1, where the solid grey represents the stationary guide vanes, or stator, the striped portion represents the rotating blades, or rotor, the arrows represent flow direction, and the dashed line represents the axis of rotation, or center of the shaft. The system can benefit from axial flow with a single symmetric rotor, also called an impulse turbine in turbomachinery. With opposite facing stators on each side of the rotor with angled, nozzle-like guide vanes, the flow can be directed through the rotor in either direction depending on the pressure differential, while maintaining the direction of rotor rotation. With the ability to operate in reverse, pressure energy could be harvested as a marine species performs a complete dive cycle, therefore increasing the available power to the tag, as discussed in Section 2.3. Although an accumulator-style system is the proposed end goal for this application, this research focuses on the analysis and characterization of the scaled axial, impulse turbine, independent of the overall reversible system.

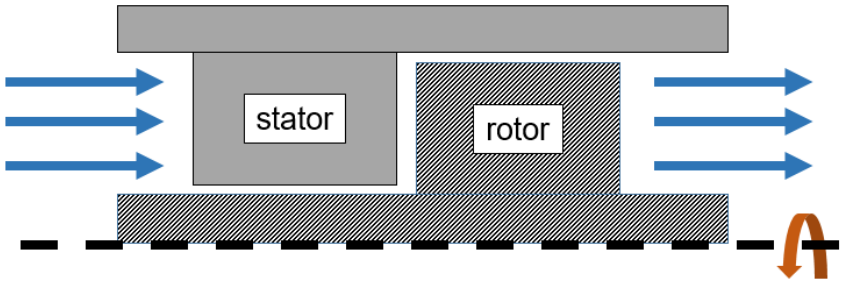


Figure 3.1: Diagram showing flow direction through an axial turbine with a single stator and rotor.

## 3.2 Graphical modeling

Axial impulse turbines are a common type of fluid machinery and the basic analytical relationship between a stator vane and rotor blade has already been defined in scientific literature. This relationship is comprised of the velocity components of the fluid and moving rotor blades, providing insight into the most optimal design. Optimal design, in this case, refers to stator vanes and rotor blades of specified geometries that allow the system to operate most efficiently for some corresponding jet velocity and rotational velocity.

Figure 3.2(a) displays the velocity components and geometric properties of the control volume for a single stator and rotor vane. The fluid enters the stator vane at absolute velocity $V_1$ and exits at velocity $V_2$ (jet velocity) in a direction relative to the angle of the stator vane ($\alpha_2$). The jet velocity to the control volume moving with the rotor blade, moving at speed $U$, is identified as the relative jet velocity ($W_2$). The speed of the rotor blade is a function of the rotational velocity ($\omega$) and position along the radius ($r$). The angle of $W_2$ ($\beta_2$) is a function of the blade speed, while the direction of the relative velocity leaving the rotor ($W_3$) stays constant corresponding to the rotor blade angle ($\beta_3$). The jet of fluid, of horizontal width $b$ and cross-sectional

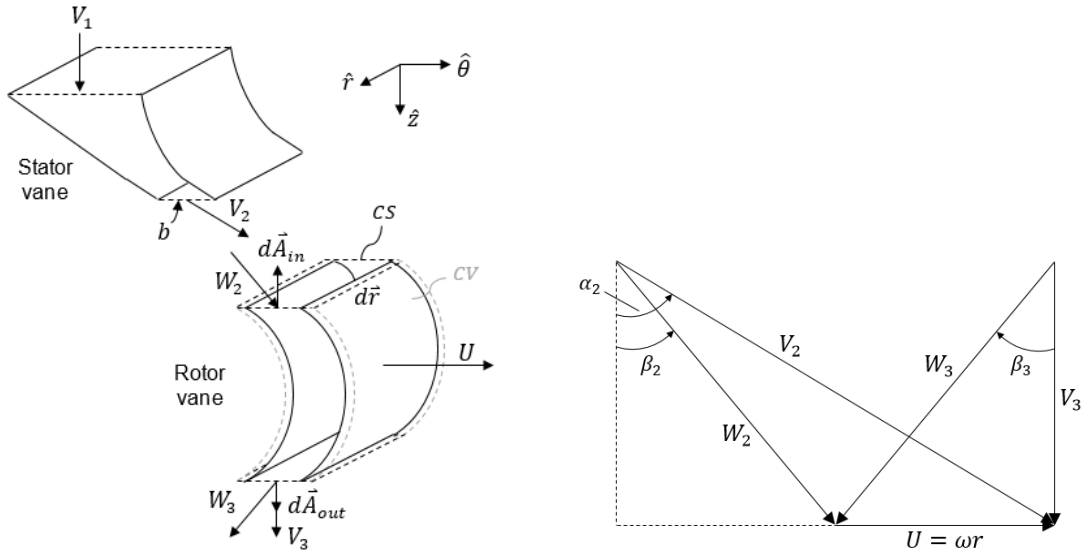


Figure 3.2: Diagram of (a) the control volume and (b) relationship between velocity vectors.

area $A$, enters and leaves the rotor vane, assumed to stay constant in size. The two-dimentional relationship between the velocity components shown entering and leaving the control volume and their corresponding angles is presented in Figure 3.2(b) [37]. This figure represents the optimum velocity diagram for an axial, impulse turbine, defined when $|W_2| = |-W_3|$. At this position, neither the blade speed nor the force on the blades are at their max. As blade speed increases, the force on the blades decreases. Therefore, at the position shown in the velocity diagram, half the speed and half the force, the maximum power output is achievable, as the power output is the multiplication of the rotational velocity and torque on the shaft.

## 3.3 Analytical model of energy transfer

Once the relationship between the fluid velocity components from the stator to the rotor is understood, the transfer of energy from the fluid to the rotor blades can be explained analytically in terms of torque on the shaft ($\vec{T}_{shaft}$). This can be found through the application of the Reynolds Transport Theorem to the conservation of angular momentum for an inertial, constant velocity control volume, as shown in Equation 3.1 [38].

$$\vec{r} \times \vec{F}_s + \int_{CV} \vec{r} \times \vec{g} \rho d\,V + \vec{T}_{shaft} = \frac{\partial}{\partial t} \int_{CV} \vec{r} \times \vec{V} \rho d\,V + \int_{CS} \vec{r} \times \vec{V} \rho \vec{V} \cdot d\vec{A} \tag{3.1}$$

For this system, several terms are assumed to be negligible, such as surface forces ($F_s$) and gravitational forces ($\vec{g}$). The turbine is also assumed to have reached steady state, eliminating any time-dependent terms. Equation 3.1 simplifies to

$$\vec{T}_{shaft} = \int_{CS} d\vec{T}_{shaft} = \int_{CS} \vec{r} \times \vec{V} \rho \vec{V} \cdot d\vec{A} \tag{3.2}$$

where the radius of the vane ($\vec{r}$), the fluid velocity ($\vec{V}$), and the fluid density ($\rho$) are integrated over the control surface ($CS$) in the radial direction. The expansion of the fluid velocity vector into components of the relative velocities entering and leaving the control surface results in Equation 3.3.

$$d\vec{T}_{shaft} = r \times \rho \left[ (W_{2\theta} W_{2z} + W_{2z}^2) d\vec{A}_{in} + (W_{3\theta} W_{3z} + W_{3z}^2) d\vec{A}_{out} \right] \tag{3.3}$$

Equations 3.4a - 3.4d represent the relative velocities all in terms of the jet velocity

using the geometric relationship shown in the velocity diagram (Figure 3.2(b)) of the previous section.

$$W_{2\theta} = V_2 \sin \alpha_2 - \omega r \tag{3.4a}$$

$$W_{2z} = V_2 \cos \alpha_2 \tag{3.4b}$$

$$W_{3\theta} = -V_2 \cos \alpha_2 \tan \beta_3 \tag{3.4c}$$

$$W_{3z} = V_2 \cos \alpha_2 \tag{3.4d}$$

The velocity diagram indicates that $\beta_2$ is a function of the blade speed and will therefore equate to different angles along the radius at a constant speed. At the optimum operating point, the angle of the rotor blade should match the relative velocity angles on the inlet and outlet. This means that $|-\beta_3|$, which is equal to $|\beta_2|$ at this point, is varying along the radius as well. Therefore, Equation 3.4c must be expanded further in order for the integration to properly take place. The geometric relationship for $\beta_3$ at the optimum operating point is defined as

$$\beta_3 = \tan^{-1}\left(\frac{U_{opt}}{W_{3z}}\right) = \tan^{-1}\left(\frac{\omega_{opt} r}{V_2 \cos \alpha_2}\right) \tag{3.5}$$

where the mean radius ($r_m = \frac{r_2 + r_1}{2}$) is used to find the optimum rotational velocity ($\omega_{opt} = \frac{U_{opt}}{r_m}$). The optimum blade velocity ($U_{opt}$), representing the unchanging $U$ in the velocity diagram, can be related to jet velocity using the diagram, resulting in

$U_{opt} = \frac{V_2 \sin \alpha_2}{2}$. Instead of a constant rotor blade angle, this relationship describes a rotor blade angle that changes along the radius to provide a design that operates at an optimal speed for a given, constant jet velocity magnitude and direction. Due to pressure driving the velocity of the fluid, each pressure will result in a different optimal operating point, torque and speed, of the turbine.

Expanding the area as a function of radius for the fluid entering and leaving the rotor vane results in $d\vec{A}_{in} = -bdr\hat{z}$ and $d\vec{A}_{out} = bdr\hat{z}$. Integration over $r$ and simplification results in Equation 3.6 for the total torque on the shaft, where n is the number of stator vanes or number of jets impacting the rotor. The inner and outer radii of the vane are represented by $r_1$ and $r_2$, respectfully.

$$T_{shaft} = -\rho b \mathrm{n} \left[ -V_2^2 \left( \frac{r_2^2 - r_1^2}{2} \right) \sin \alpha_2 \cos \alpha_2 + V_2 \omega \left( \frac{r_2^3 - r_1^3}{3} \right) \cos \alpha_2 \right. \\ \left. - V_2 \omega_{opt} \left( \frac{r_2^3 - r_1^3}{3} \right) \cos \alpha_2 \right] \tag{3.6}$$

The system efficiency can then be assessed by comparing the available power from the fluid energy source to the power output from the turbine shaft. In mathematical form, the mechanical efficiency, $(\eta)$, can be expressed as

$$\eta = \frac{\text{power out}}{\text{power in}} \times 100 = \frac{T_{shaft} \cdot \omega}{\Delta p \cdot Q} \times 100 \tag{3.7}$$

where $\Delta p = p_1 - p_2$ is the pressure difference across the system with $p_1$ as the pressure at the inlet, upstream of the stator, and $p_2$ as the pressure at the outlet, downstream of the rotor, assuming no pressure drop occurs across the rotor, and $Q$ is the volumetric flow rate.

An important purpose of this analytical model is to ultimately predict the power output and efficiency of the design for a given pressure. Therefore, jet velocity should be expanded further to incorporate pressure as a model input, assuming flow rate is unknown. As a first order estimate, the velocity of the fluid exiting the nozzle-like stator vane can be calculated using the Bernoulli's equation. Equation 3.8 displays a simplified version of the equation where the assumptions are that the nozzle inlet velocity is negligible and the potential energy per unit volume is equal at the inlet and the outlet.

$$V_2 = \sqrt{\frac{2\Delta p}{\rho}} \tag{3.8}$$

The model in its form as of now presents an ideal system that operates at 100% efficiency. However, research has shown that this is impossible to achieve in real-world applications and specifically with turbines or like-systems, where efficiency tends to decrease with size. Literature has presented ways of quantifying losses for mostly large-scale systems. However, this is usually followed by and verified with testing of a physical prototype. For a system on a much smaller scale, testing is necessary to aid in the quantification of these losses, which will be a much more significant fraction of the overall energy conversion than would be expected for larger systems. Known loss coefficients, such as those characterized for flow entrances and exits, may also only be applicable to the large-scale systems. In a later chapter, after presentation of the experimental methods, the loss analysis methods from literature, as well those identified from testing of the physical prototype, will be discussed further and applied to the model for validation.

## 3.4 Summary

This chapter defined the proposed turbine design as an axial impulse turbine involving a stator with nozzle-like vanes and a rotor with symmetric blades. Geometric properties and a corresponding velocity diagram were established and displayed graphically using basic turbomachinery methods. Key features, such as blade angle, were explained in depth, along with their relationship with the relative velocity. The energy transfer of the moving fluid to the rotor shaft was then expanded mathematically with the application of the Reynold's Transport Theorem to the conservation of angular momentum for inertial control volume. This resulted in an equation for the torque on the shaft with key inputs such as nozzle angle, radii, rotational speed, and jet velocity, calculated using the pressure drop. Finally, the equation for finding the mechanical efficiency of the system was defined.

# Chapter 4

# Experimental Methods and Results

A prototype of the turbine was developed to assess the efficiency of the presented design concept. The beginning stages of prototype development with experimental testing unfolded in parallel with the analytical model to aid in the understanding of various sources of loss in the design. The experimental setup and evolution of the rotor and stator is presented, followed by the experimental results of the optimized design.

## 4.1 Experimental setup and testing parameters

In order to understand the evolution of the turbine design, the experimental setup is first explained, as the design changed based on the results of each test. However, the test housing did not change significantly throughout turbine development. A computer generated model of the prototype and section view of the test housing is shown in Figure 4.1. The flow enters through an inlet near the bottom of the housing, the stator nozzle-like vanes direct the flow to impact the rotor blades, and the flow

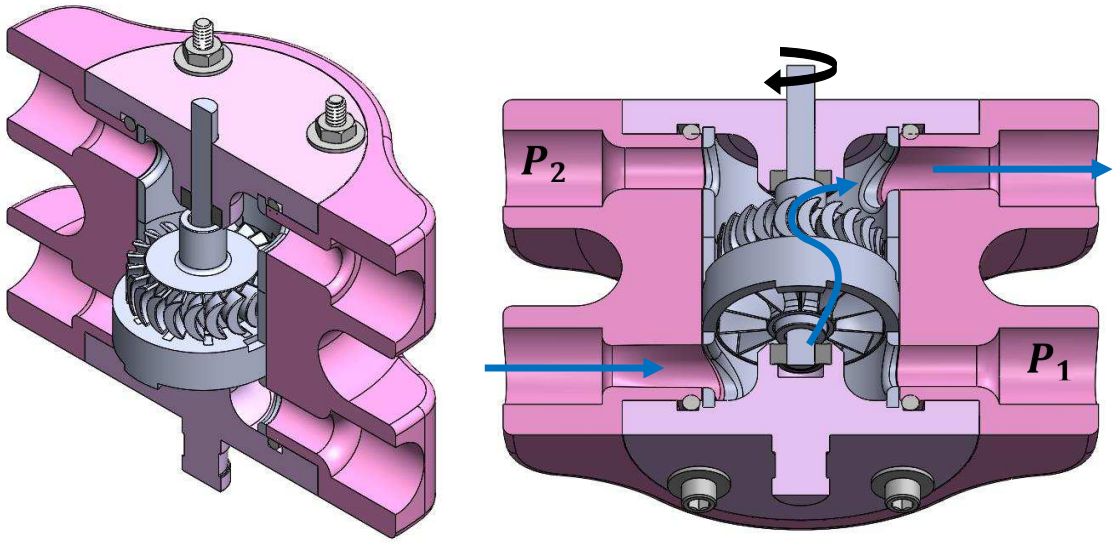


(a) (b)

Figure 4.1: SOLIDWORKS® rendering of prototype assembly used for testing, showing (a) section view of internal components and (b) direction of fluid flow.

exits the housing through an outlet near the top. The internal diameter of the housing was chosen based on the thickness of common pinniped telemetry tags from Wildlife Computers™ ($< 25$ mm). The exact number is an approximation, yet similar to the size of a U.S. quarter, and could be easily adjusted for the chosen application.

The diagram in Figure 4.2 displays the experimental setup used to obtain torque, angular velocity, pressure, and flow rate measurements from the turbine. These measurements are needed to assess the mechanical efficiency and power output of the turbine. Two OMEGA® PX309-015GI pressure transducers were used on each end of the housing to measure the pressure across the stator-rotor assembly. An OMEGA® FTB604B flow sensor was used to measure the volumetric flow rate exiting the system. The data sample rate was 1 Hz and was processed and recorded with National Instruments™ data acquisition (DAQ) technology and LabVIEW software. The

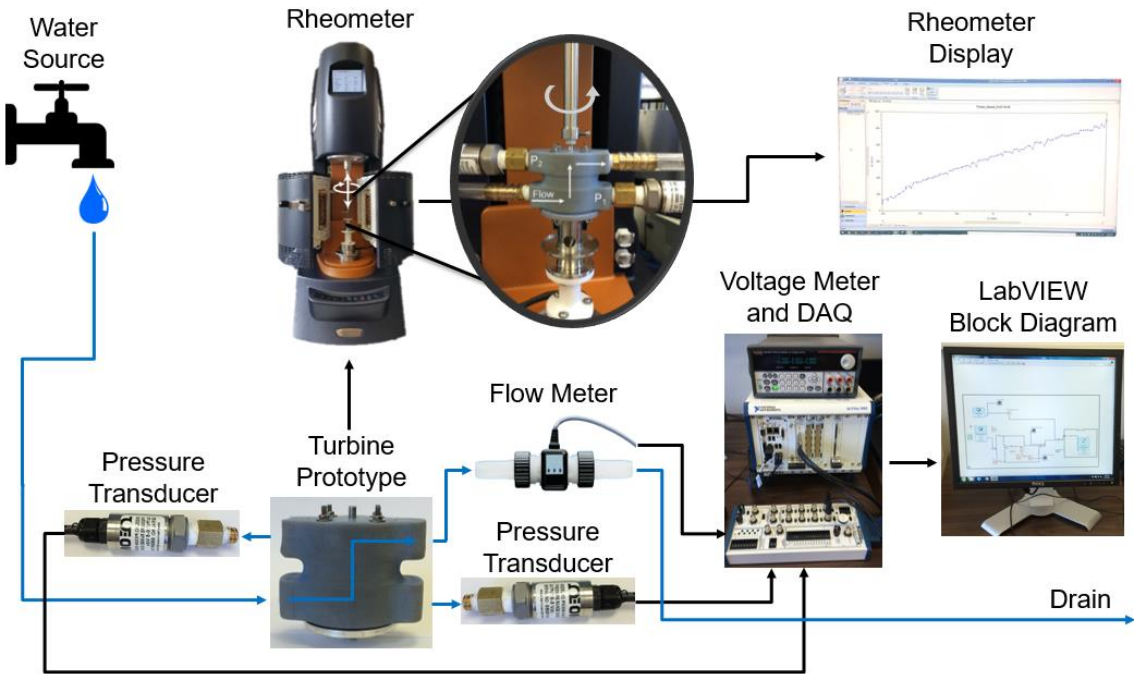


Figure 4.2: Diagram of experimental setup.

Discovery Hybrid Rheometer HR-2 by TA® Instruments was used to measure the torque on the shaft and corresponding rotational velocity. A rheometer can be used to measure various forces, displacements, temperatures, etc. to characterize fluids or materials. The device is highly sensitive and accurate, as well as technologically advanced with the ability to create intricate transient test plans. Specifications of the equipment used are summarized in Table 4.1.

Table 4.1: Equipment specifications.

| Device | Measurement Type | Range | Resolution/ Accuracy |
|---|---|---|---|
| Rheometer | Torque | ±200 mN·m | 0.1 nN·m |
| | Angular Velocity | ±300 rad/s | - |
| Flow Sensor | Volumetric Flow Rate | 1.0 - 30 L/min | ±1% of reading |
| Pressure Transducer | Gage Pressure | 0 - 15 psi | ±0.25% static |

Although the rheometer is limited to 300 rad/s, insight into the initial performance of the turbine could be captured with this device. The rheometer accessory shaft was coupled to the eighth-inch diameter output shaft of the turbine with a flexible, custom coupling. The prototype, supplied with a constant flow of water, spun freely while the rheometer was not applying an opposing torque, also known as no-load speed. The test plan in the rheometer interface was designed to have the rheometer shaft speed match the no-load speed of the turbine at the start of the test and then step down in speed until both the rheometer and turbine were brought to rest. While the flow was still constant, but the turbine was forced to rest, the maximum torque the turbine was experiencing was measured. This is referred to as the stall torque. As speed decreased at increments of 2 rad/s, the rheometer dwelled at each increment for approximately 7 seconds. The resulting torque measurement at that speed is the average of the seven data points collected during the dwell time. The fluid flow was controlled by a small pump with a DC controller that provided the capability to adjust the flow rate as desired.

## 4.2 Prototype development

The turbine prototype, as well as the test housing, was created by 3D printing for initial testing, as printing provides the flexibility to modify designs at a low cost and minimal time expenditure. Variations of the turbine components include a number of geometric parameters that were adjusted as understanding of the velocity diagram progressed. A large contribution to the modeling efforts was also the understanding of the tools available, such as computer-aided modeling (CAD) and measurement devices. The goal of each modification was to improve the effect key parameters had

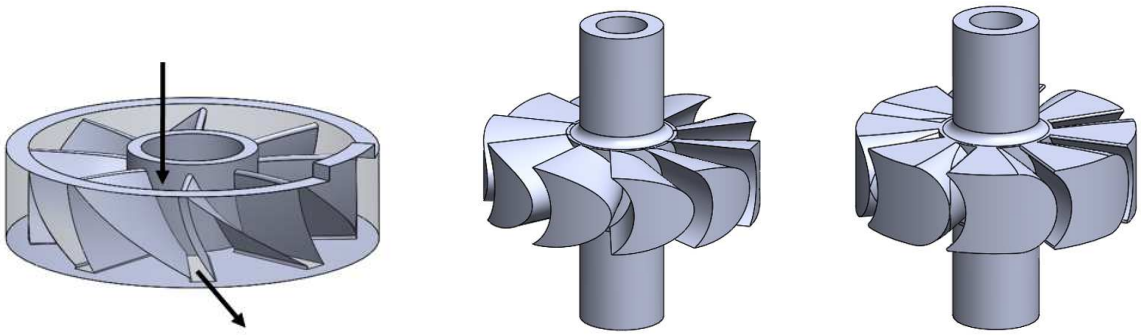

(a) (b) (c)

Figure 4.3: Models of turbine components in the early stages of development: the (a) stator, (b) curved rotor, and (c) flat blade rotor.

on the efficiency of the turbine.

### 4.2.1 Preliminary designs and losses

One of the first rotor designs is shown in Figure 4.3(b). The rotor had 10 blades and a constant blade angle ($\beta$) of 60°. This was tested along with the stator shown in Figure 4.3(a), which had eight vanes. At the time of development, the vane outlet was assumed to be at an angle ($\alpha$) of 60°. However, it was later discovered that the angle was not constant due to the CAD modeling method used to create the nozzle-like vane feature, resulting in an uncontrolled, varying angle along the radius. The results from this design included a maximum mechanical power output of 75 mW and 8% efficiency for a pressure drop of 1.45 psi and flow rate of 5.4 L/min. While analytical modeling was in works parallel to testing, a modification was made to the rotor design presuming it would simplify the analysis as well as manufacturing. The blade number was decreased to eight blades with a constant width between the blades, as shown in Figure 4.3(c). This design decreased the efficiency to 6% and as a result of the

new blade shape with a flat top surface and sharp edge vane entrance, the flow rate decreased to 4.8 L/min for a slightly higher pressure drop 1.7 psi.

The flat top surface of the blades caused significant obstruction of the fluid exiting the stator nozzles. As the rotor rotates and each blade passes a jet of fluid, the fluid is temporarily blocked from fully impacting the rotor blade. Figure 4.4(a) highlights the top surface area of the blades from the rotor in Figure 4.3(c), which shows the significant size of the blade area compared to the vanes. For one revolution, the eight rotor vanes are completely aligned with the eight jets of fluid leaving the stator vanes only 40% of the time, not including the partial jet impact as the rotor rotates. During the other 60%, the jets are presumed to be completely blocked by the blade. To estimate the effect of obstruction with partial jet impact included, the average can be taken of the ratio of jet fluid passing clearly through a vane to the jet fluid that may be blocked by the blade's surface during a single rotation, thus creating a duty cycle pattern. To further explore the effects of this loss, the same rotor design was tested with an increased space between the blades, approximately 1 mm to 1.5 mm, as shown in Figure 4.4(b), decreasing the surface area of the blades to approximately 50% of the total area. The design resulted in 85 mW for a pressure drop of 1.1 psi and 5.8 L/min and the efficiency almost doubled to 11%. This demonstrates that with less obstruction, more fluid is able to pass through the system without affecting the pressure drop, ultimately resulting in a higher efficiency.

During all tests up to this point, there were other factors involved that increased the uncertainty of the experimental results. The pressure transducers initially used were capable of measuring pressure up to 300 psi. This resulted in a significant error as tests were conducted within 0.5% of this range. The rate of fluid flow was also not

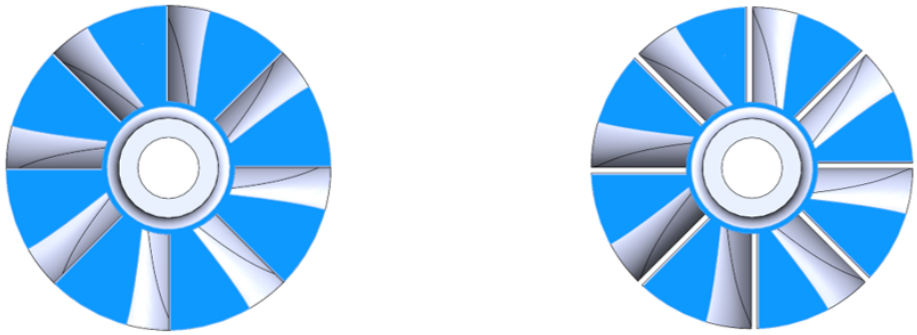

(a) (b)

Figure 4.4: Rotor blade surface area compared to vanes for an eight blade rotor with (a) a 1 mm vane width and (b) a 1.5 mm vane width. Note the eight vane stator, not pictured here, has an outlet vane width of 1 mm.

constant during testing because the fluid source was directly from the lab's faucet, which is dependent on the provided pressure of the facility. Apart from equipment uncertainty, the prototype housing also resulted in uncertainty. During testing, excessive leaking was observed where the shaft extends out of the housing. This may have had a significant affect on the downstream pressure and flow rate measurement. For the design iterations to follow, the transducers and fluid source were replaced with the equipment specified in the previous section, 0-15 psi transducers and recirculating pump, respectively. To address the leaking issue, the clearance between the shaft and the housing was minimized enough to significantly reduce the leaking without causing rubbing between the components.

### 4.2.2 Secondary design and losses

As the analytical model developed further, another change was made to the stator and rotor design. The blade and vane lengths were reduced to lessen the dependency on the radius and continue with a two-dimensional analysis of the flow through the

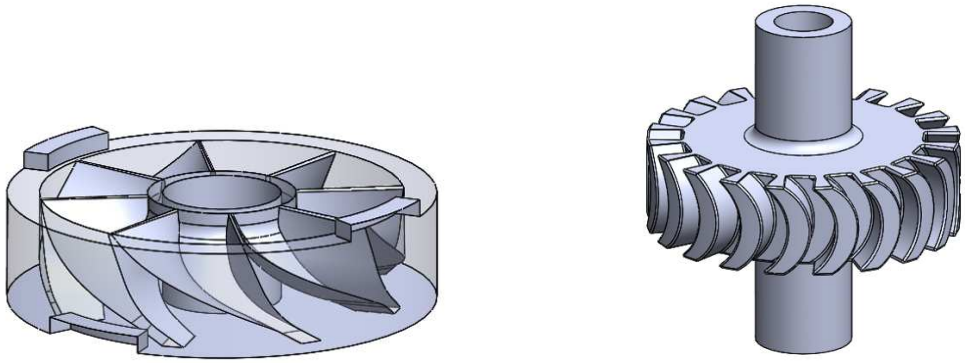

(a) (b)

Figure 4.5: The next iteration of the (a) stator and (b) rotor design with reduced vane and blade length.

system, ignoring pressure gradients along the blades radially. The stator was rebuilt with 10 vanes and included a controlled vane outlet angle of 60°, as shown in Figure 4.5(a). The rotor blades remained 60°, but the number of blades was increased to 20, as shown in Figure 4.5(b). The design testing resulted in 49 mW of power output and 4.1% efficiency at 4.3 psi and 2.4 L/min. The decrease in efficiency from the previous design was a result of the decreased blade length. The input fluid was no longer capable of contributing as much to the momentum of the blades due to the decreased blade surface. This also ultimately accentuated losses that will be discussed in a later section.

To observe the effects of obstruction for this configuration, a test was conducted without the rotor installed to capture the pressure and flow rate across the stator only, which represents the data we should see if obstruction and viscous losses from the rotor were minimal. The data, presented in Figure 4.6, showed an increase in flow rate through the stator, as the fluid was able to pass through more easily for the same amount of pressure drop. The ratio of fluid able to pass through, approximately

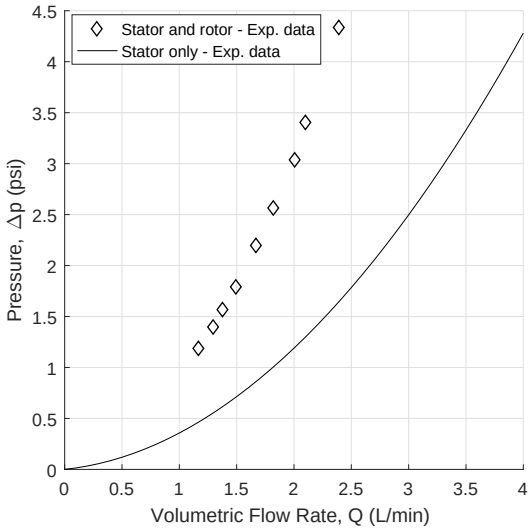


Figure 4.6: Comparison of pressure and flow rate from the system experimental results and the system without the rotor installed.

65%, was applied to the flow rate of the stator test, which then matched closely to the system experimental data. The test confirmed the significant effect blade obstruction has on the available input flow, subsequently the jet velocity and efficiency, which identified a location for improvement in the future designs. As understanding of the analytical model progressed, it was realized that a constant width between blades is not necessary, and therefore the next design reverts back to the original rounded blade design from Figure 4.3(b).

Another flaw in this design is the angle of the stator vane and rotor blade. The angles were equal for this design, which is confirmed to not be optimal according to the velocity diagram. The angle of the stator vane shall be modeled such that the angle of the *relative* jet velocity is equal to the rotor blade angle at the optimum blade speed. The stator angle was also constant across the radius, which is not optimal, yet fair for the blade length compared to the full radius of the rotor and a fine assumption

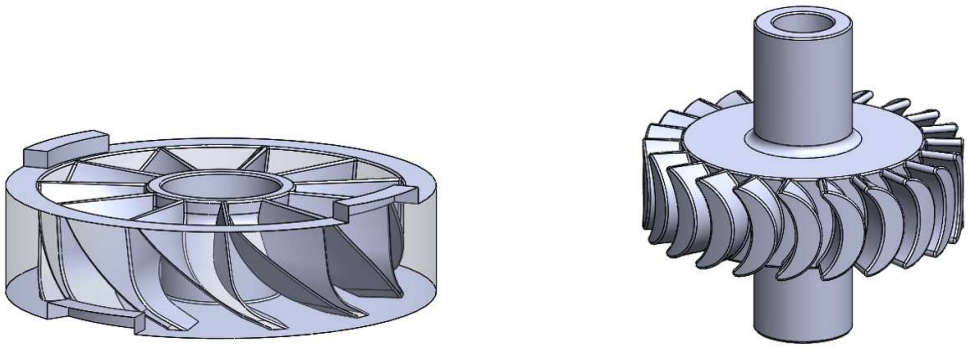

(a) (b)

Figure 4.7: The final iteration of the (a) stator and (b) rotor design with reduced vane and blade length.

for 2D analysis. However, the angles for the new design follow the guidelines of the velocity diagram more closely by implementing the correct angles along the radius for optimal speed. In addition to blade shape and angle, the clearance between the stator and rotor was accounted for, as it might affect how the angled jet impacts the rotor. By acknowledging and reducing the clearance in the new design, the stator angle was designed slightly more steep for an increase in fluid velocity leaving the nozzle-like vanes.

### 4.2.3 Final design

Using what was learned from the previous designs, the configuration shown in Figure 4.7 was created and is used for the remainder of this paper. The angle of the rotor blade, as discussed, increases linearly along the radius. The number of blades was maximized based on the printer resolution and suggested minimum thickness for structural strength of the blades, in addition to the desired vane width of at least 1 mm. The number of stator vanes was decreased by a factor of 2 in order to maintain

Table 4.2: Geometric properties.

| Variable | Stator vane | Rotor |
|---|---|---|
| $r_1$ | 6.4 mm | 6.4 mm |
| $r_2$ | 8.4 mm | 8.4 mm |
| $b$ | 1 mm | 1 mm |
| $\alpha_2$ | 65° | - |
| $\beta_2$ | - | 42.8°at $r_1$; 50.6°at $r_2$ |
| $\beta_3$ | - | -42.8°at $r_1$; -50.6°at $r_2$ |
| # of vanes | 11 | 22 |
| height | 5 mm | 5 mm |

the nozzle feature that directs and increases the velocity of the fluid flow. The key variables of the prototype design are defined in Table 4.2.

The physical turbine components, shown in Figure 4.8, were created with a Stratasys Objet30 3D printer with VeroClear material using a PolyJet printing method. This method is known for its ability to produce small features with high resolution. Also, the process, which involves the layering of curable liquid photopolymer, results in a more fine texture, when compared to techniques such as Fused Deposition Modeling (FDM). However, the resolution, accuracy, and surface finish are all dependent on the positioning and features of the part. The nonporous VeroClear material used is sufficient for initial testing, as it is rigid and strong enough to withstand moderate pressure and high speeds.

(a) (b)

Figure 4.8: Physical model of turbine components: (a) rotor and (b) stator inlet (left) and outlet (right).

## 4.3 Experimental results and discussion

Multiple data sets were collected to capture the torque-speed curves at various pressure differences across the system, as shown in Figure 4.9(a). The flow rate was adjusted evenly using the DC voltage controller between each test to provide this range of data. These results show performance that aligns well with what would be expected for a power generating hydrokinetic turbine of this type, including linear torque-speed curves, suggesting standard modeling methods. The mechanical power output, calculated from the torque and rotational velocity, is shown in Figure 4.9(b). Recall the mechanical efficiency, shown in Figure 4.9(c), of the turbine is the actual amount of power output from the shaft compared to the given input power from the pressure and flow rate of the fluid. A maximum of approximately 57.5 mW at 9% efficiency was reached with a $\Delta p$ of 1.92 psi, which is double the efficiency at half the differential pressure compared to the previous design.

When comparing the maximum power and mechanical efficiency of the turbine for a range of $\Delta p$, an increasing trend can be seen, as shown by Figure 4.10(a). These

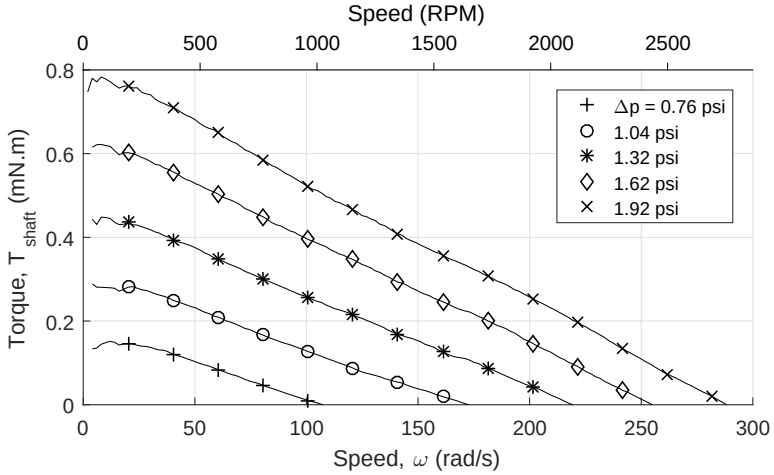


(a)

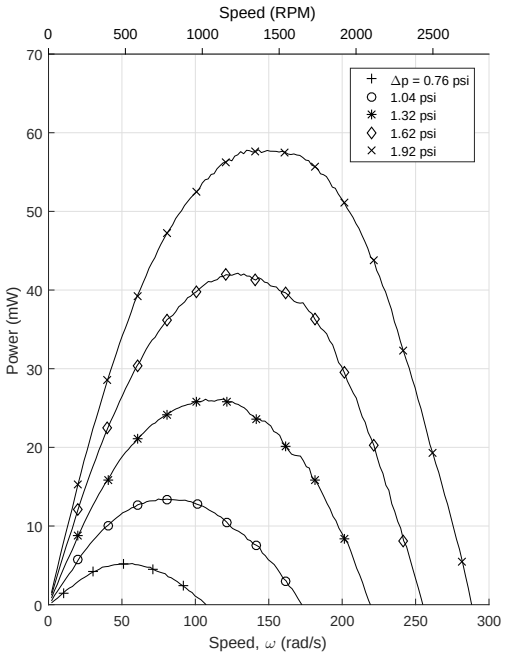


(b)

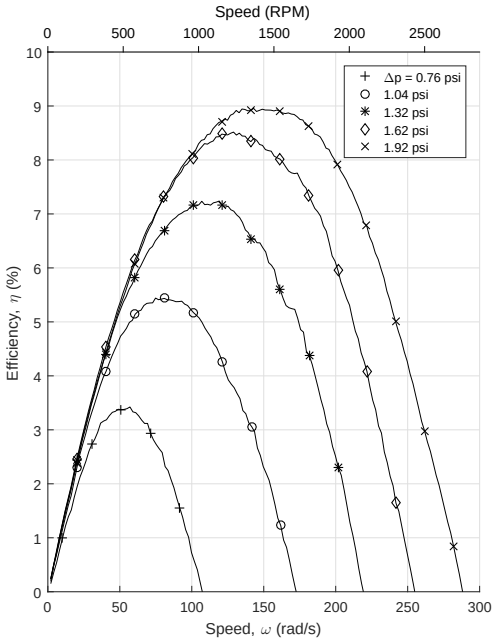


(c)

Figure 4.9: (a) Experimental torque-speed curves at various pressure differences across the turbine and corresponding (b) power output from the turbine shaft and (c) mechanical efficiency.

results were limited to the capability of the rheometer, yet the trend shows that there is potential for higher power output given a greater pressure differential. Also shown in the figure for reference is the uncertainty of the efficiency due to the accuracy of the flow rate and pressure measurements. This is not included for power as the resolution of the rheometer for torque and speed is very high, making the error negligible. Figure 4.10(b) displays the maximum power and efficiency with the corresponding rotational velocity of the turbine. The speed measured at each maximum is the optimum speed for that given flow rate or measured pressure differential. The efficiency appears to be approaching an overall maximum for the system at given pressure differentials, yet increasing linearly when comparing to optimum speed, except for the highest data point. It is possible that the highest test point is outside of the trend due to an unidentified error in experimental testing. With a single point slightly outside of the trend and not having enough data, the maximum efficiency for the system cannot be confirmed at this time. However, with further higher pressure tests, the maximum can continue to be explored.

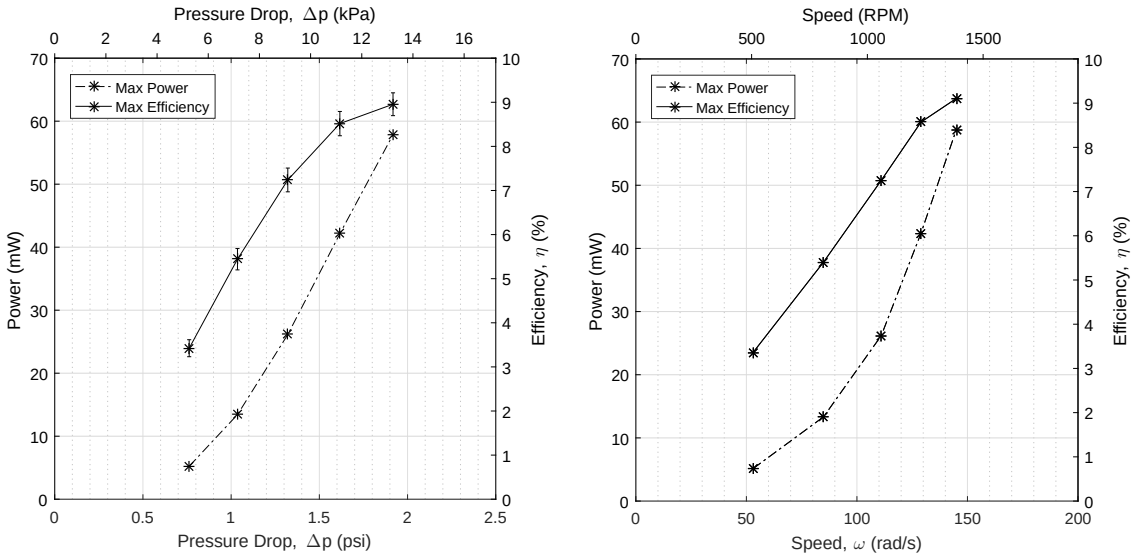


(a) (b)

Figure 4.10: Maximum power and mechanical efficiency per each (a) pressure differential test and (b) corresponding optimum rotational velocity.

## 4.4 Summary

Within this chapter, the experimental methods and results of physical prototype testing of the proposed turbine design were presented. A rheometer was used to directly measure the shaft torque and rotational velocity for various flow rates. Pressure and flow rate were measured to determine the pressure drop across the system and assess the efficiency of the turbine. The 3D printed protoype parts had undergone various design changes as testing and analysis highlighted uncertainties and losses that could be addressed and mitigated for future designs. These losses or uncertainties included effects of improper modeling of the geometry, blade obstruction, and measurement device accuracy. The current, most optimized design was further defined and the experimental results of five different pressure differential tests were presented. The

results showed a maximum mechanical power output of 57.5 mW and 9% efficiency for only 1.92 psi across the system. The results were further analyzed to show an increasing trend in both power and efficiency.

## Chapter 5

# System Losses

The accuracy of the analytical model presented in Section 3.3 is validated by a comparison with the experimental data. While several losses were identified with past designs, the experimental results show there are additional losses not yet accounted for or quantified for this design. The losses to be discussed include minor head loss in the stator entrance and exit, as well as from abrupt changes in area within the system, clearance loss referring to internal leakage, viscous loss from fluid between rotating parts, experimental losses, and physical modeling uncertainties. These losses are discussed further here and applied to the model for comparison.

## 5.1 Flow coefficient

As previously stated, the model as it is presented now represents an ideal system with pressure drop as the input, assuming flow rate is unknown. Since we know the system is not ideal, or 100% efficient, an attempt can be made to estimate the losses using known turbomachinery analysis methods. However, through this it was

discovered that these methods may not yield an accurate result, as the losses are magnified for systems on the scale of millimeters. For example, an initial attempt was made to approximate the loss in the pressure drop across the stator, which would normally be captured by a measured flow rate. This approximation involved the commonly known nozzle discharge coefficient equation, which accounts for the losses experienced through a nozzle. The discharge coefficient ($c_d \leq 1.0$), or correction factor, was estimated using the correlating equation, Equation 5.1 [37].

$$c_d = 0.9965 - .00653 \left(\frac{10^6}{Re}\right)^{1/2} \tag{5.1}$$

This coefficient is applied directly to the simplified Bernoulli's equation, as shown in Equation 5.2.

$$V_2 = c_d \sqrt{\frac{2\Delta p}{\rho}} \tag{5.2}$$

Reynold's number ($Re$) is calculated by $Re = \frac{V_2 d}{\nu}$ where $d$ is the hydraulic diameter and $\nu$ is the kinematic viscosity of the fluid. While velocity and the coefficient are unknown, an initial guess is made for the coefficient and then corrected iteratively using all three equations until the $c_d$ value converges within a set tolerance. The resulting coefficient varied little between the tests with an average of $c_d = 0.956$.

Since the flow rate was measured during the prototype experiment, a comparison can be made between the ideal value, the corrected value, and the measurement. It is important to note that the measurement was taken across the system, the stator and rotor. The flow rate and pressure drop across the stator was tested experimentally and showed little variation when compared to that of the entire system. This means

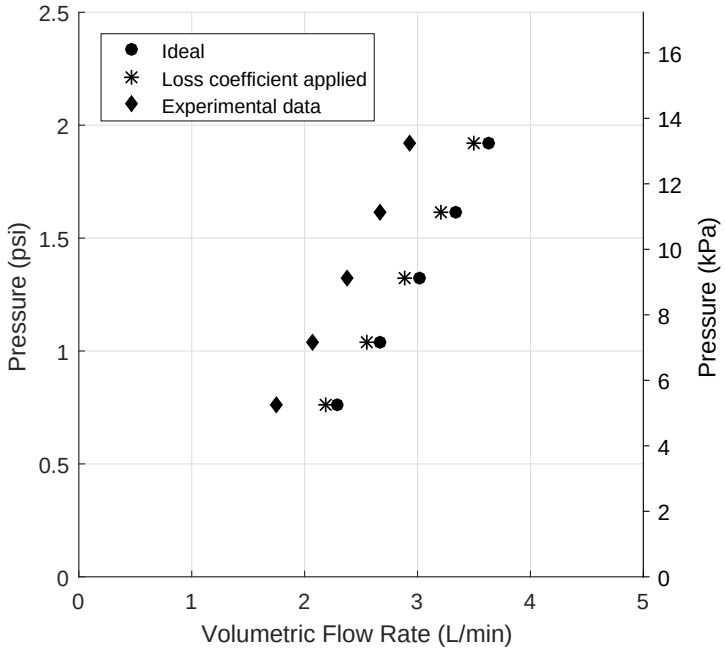


Figure 5.1: Comparison of the flow rate and pressure drop relationship for the ideal state, the corrected result, and the experimental data.

obstruction losses were minimal and the majority of the pressure drop occurred across the stator as assumed. Therefore, the system measurement can continue to be used for comparisons. Figure 5.1 shows the significant error between the corrected value and the measurement. This demonstrates the difficulty in determining which known analysis methods are applicable to systems on this scale. However, this is also understood considering the configuration of the prototype nozzle is not a replica of common nozzle designs, such as those that provided the empirical data for the creation of the correlating equation. Also, the addition of the rotor likely causes additional losses in the flow. Literature has expressed how determining a coefficient that applies to nozzles or flow configurations of all sizes is unattainable [38]. A vast amount of experimental data has been used to correlate common flow configuration losses, yet these

values remain known as a general estimate. In many cases, different sources have obtained different values for the same configuration. Therefore, it is recommended that any loss coefficient be determined experimentally for each situation. This can be accomplished with the steady state energy equation for incompressible pipe flow [38]. Using the same assumptions as those defined earlier for the Bernoulli's equation and ignoring friction losses, the following equation remains.

$$\frac{\Delta p}{\rho} - \frac{V_{2-measured}^2}{2} = h_m = K\frac{V_{2-measured}^2}{2} \tag{5.3}$$

The variable $h_m$ represents the minor head loss which includes the loss coefficient ($K$). This coefficient encompasses the viscous losses in the flow channels throughout the system, including any losses due to abrupt changes in area. The variable $V_{2-measured}$ used in this equation is the nozzle exit velocity calculated from the measured flow rate. This calculation in its basic form is the measured flow rate divided by the total stator outlet area, which will be defined further in the following section. The resulting loss coefficient is shown in Figure 5.2, where the nozzle discharge coefficient is also shown. There appears to be a trend to the data, exhibiting a decrease in the loss coefficient and slight increase in nozzle discharge coefficient for increasing pressure drop, indicating increasing viscous losses through the stator.

For use in the model, Equation 5.3 is rearranged to Equation 5.4 such that $K$ and $\Delta p$ are known and jet velocity is calculated. Using the trend of $K$ seen in the figure and the equation below, a prediction of the jet velocity for higher pressures may be made without known flow rate data. Yet, the best way to verify the coefficient is through additional experimental testing.

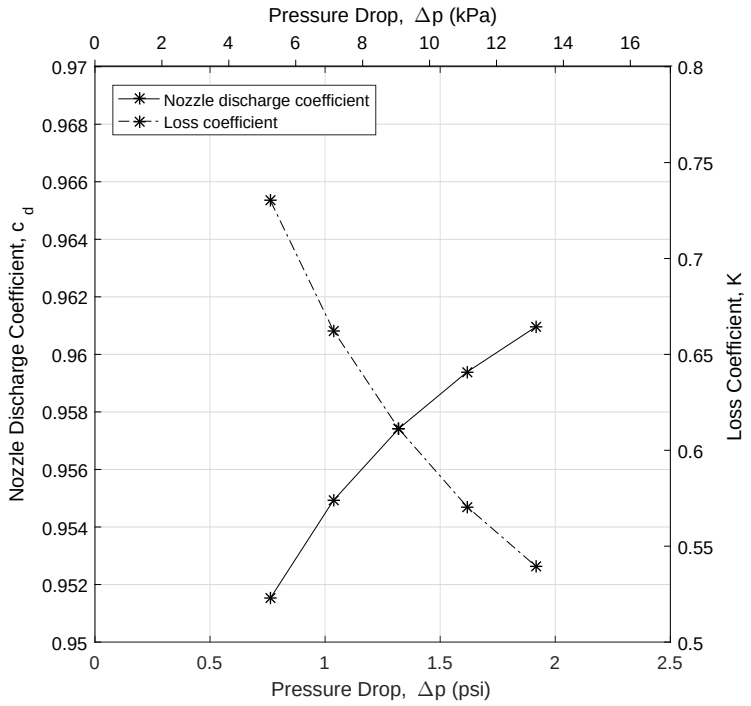


Figure 5.2: Nozzle discharge coefficient and loss coefficient calculated for each pressure differential test.

$$V_2 = \sqrt{\frac{2\Delta p}{\rho(K+1)}}. \tag{5.4}$$

## 5.2 Clearance loss

A significant source of loss in the prototype design is the clearance between parts relative to the size of the parts themselves. Although difficult to reduce in 3D printed parts, the clearance may be reduced in machined parts. Regardless, the error is simple to quantify by calculating the ratio of clearance to the vanes. In this design, there is a small clearance gap between the extension piece of the rotor, along the shaft, and the inner diameter of the stator, which allows the rotor to spin freely without rubbing.

This gap, referred to as Gap #1, accounts for approximately 21% of the total flow rate leaving the stator, at location (b), in Figure 5.3. This means only 79% of the flow is passing through the stator vanes. When calculating the velocity leaving the nozzle-like vanes, a factor of approximately 0.79 (referred to as $K_{gap}$) is applied to the measured flow rate, as shown in Equation 5.5.

$$V_{2-measured} = \frac{K_{gap}Q}{b(r_2 - r_1)\mathrm{n}\cos\alpha_2} \tag{5.5}$$

The portion of fluid passing through Gap #1 is assumed to be thrown outward between locations (b) and (c) due to the centrifugal force of the rotating body and exits through Gap #2 (the clearance between the rotor blade tips and the housing wall). Due to the fluid evading the nozzle-like vanes and moving radially outward during this transit, it is incapable of providing desired momentum transfer to the rotor blades. This fluid likely contributes instead to the overall viscous losses in the system discussed later. It is important to note Gap #2, is 5.5% larger than Gap #1. In addition to the fluid from Gap #1, this may be filled by more fluid within the rotor vanes that is pushed radially outward when rotating or due to the jet of fluid moving tangentially to the rotating blades. The overall torque is slightly reduced as a result of the fluid again not contributing to the momentum of the rotor blades. As the majority of the clearance is already accounted for in $V_{2-measured}$, a factor of approximately 0.945 (referred to as $K_{tip}$ for tip clearance loss) can be applied to the total torque.

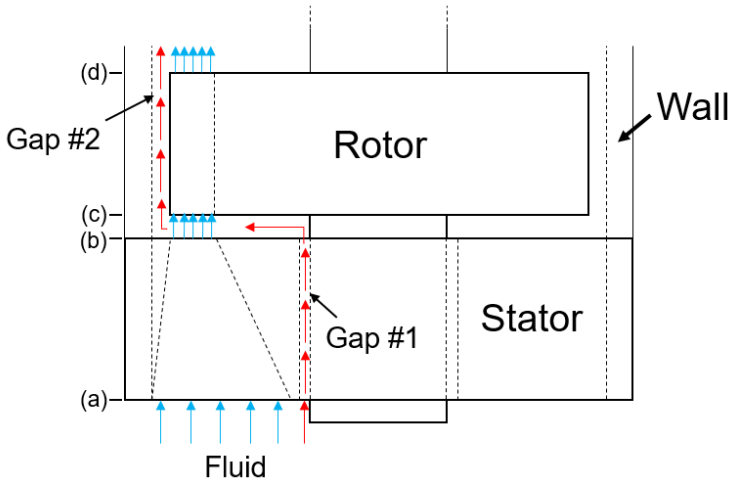


Figure 5.3: Diagram showing the direction of fluid through the system, including the vanes and clearances.

## 5.3 Viscous loss between rotating surfaces

The effect of the fluid's viscosity between rotating parts was estimated based on the shear stress ($\tau$) of the fluid and the force ($F$) it applies to the contact surfaces, resulting in a drag torque ($T$) [38]. The shear stress of the fluid is defined as $\tau = \mu\frac{du}{dy}$, where $\frac{du}{dy} = \frac{U}{b}$. The blade speed can be expanded further to $U = \omega r$. The torque is equivalent to the shear force times the radius, $T = Fr = \tau Ar$, where the shear force is the shear stress time the area ($A$) of the contact surface. The estimation of the total drag torque includes the summation of the drag torques in three areas:
the rotor extension and stator (or Gap #1),

$$T_{visc-gap1} = \frac{2\pi\mu L_{ab}\omega r_{ext}^3}{b_{gap1}}, \tag{5.6}$$

the stator outlet surface and rotor annulus,

$$T_{visc-bc} = \frac{\pi\mu\omega(r_1^4 - r_0^4)}{2b_{bc}}, \tag{5.7}$$

and the rotor blade tips and surrounding wall (or Gap #2),

$$T_{visc-gap2} = \frac{2\pi\mu L_{cd}\omega r_2^3)}{b_{gap2}}, \tag{5.8}$$

where $\mu$ is the dynamic viscosity of water, $L$ is the length of contact surface, $r_{ext}$ is the radius of the rotor extension, $r_0$ is the inner radius of the stator, and $b$ is the width of the space between surfaces. Refer to Figure 5.3 for the respective locations as they are labeled in the equations.

The total drag torque increases with rotor speed and can be subtracted as a function of rotor speed from the torque equation as $T_{visc}$. The effects are minimal as water is not a particularly viscous fluid and given the pressure used in testing, rotor speeds were relatively low. This is also based on the assumptions that the flow is laminar, steady, incompressible, fully developed, and symmetric, as well as assumed to have infinite width when comparing the length of contact and the gap between parts. These are not all accurate assumptions for this design, but allows for a rough estimate.

## 5.4 Experimental setup losses

The experiment setup itself presented additional loss. These include losses associated with the prototype bearings, rheometer bearing, coupling of the turbine shaft to the rheometer shaft, and any potential rubbing between internal components. The combined loss was measured by conducting the torque-speed test defined previously

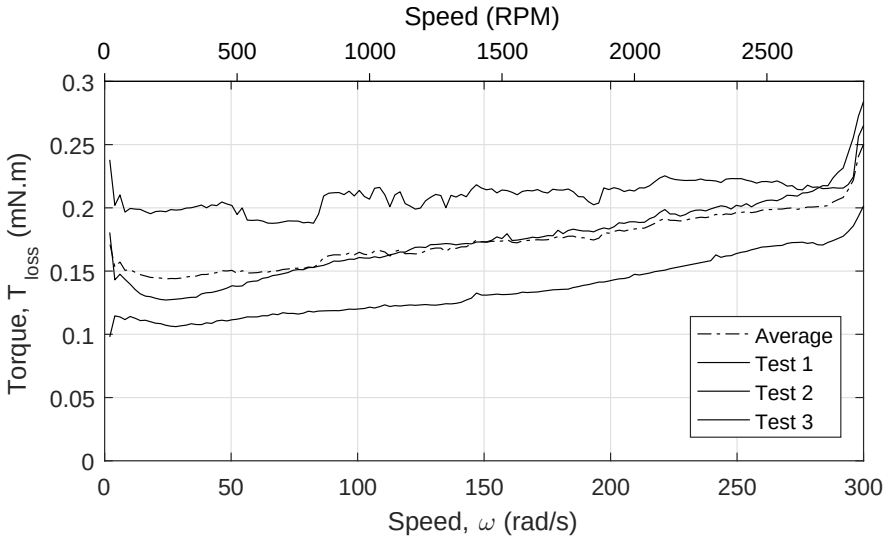


Figure 5.4: Measured experimental loss of torque over speed.

with the rheometer, however this time without providing any fluid flow. The average torque lost ($T_{loss}$) was calculated over three of these tests and is displayed in Figure 5.4. The loss, which increases slightly with speed, can be subtracted from the analytical torque equation. It is important to note that there were significant differences between each of the tests. The exact reason for this is unknown. However, a contributing cause may be a shift in alignment between tests. Any remaining water in the input and output lines or in the system may cause an unwanted force between the coupling of the shafts.

## 5.5 Results and discussion

The losses that have been identified up to this point are incorporated into the torque equation shown in Equation 5.9.

$$T_{shaft} = -\rho b \mathrm{n} K_{tip} \left[ -V_2^2 \left( \frac{r_2^2 - r_1^2}{2} \right) \sin\alpha_2 \cos\alpha_2 + V_2 \omega \left( \frac{r_2^3 - r_1^3}{3} \right) \cos\alpha_2 \right. \\ \left. - V_2 \omega_{opt} \left( \frac{r_2^3 - r_1^3}{3} \right) \cos\alpha_2 \right] - T_{visc} - T_{loss} \tag{5.9}$$

The results of the updated model are compared to the experimental data for the highest pressure drop test (1.92 psi) in Figure 5.5, where the contribution of each loss is highlighted. The largest source of torque loss, accounting for approximately 50% of the total loss, is found in the minor head loss coefficient, which also encompasses the nozzle discharge coefficient. This demonstrates that the fluid flow is significantly sensitive to the design and configuration of the system's internal components, as each channel and opening or exit shape has an effect on the overall efficiency. The most minimal contributing loss is the drag torque from the fluid between rotating parts. This is likely due to the rough estimation, in addition to the low viscosity of the fluid and relatively low rotor speeds. If the estimation assumed turbulent flow instead of laminar, higher viscous losses would be seen due to the higher velocity gradients within the boundary layers. The over-simplified viscous loss estimate would benefit greatly from CFD analysis as the loss could be properly quantified.

The model was applied and compared for each experimental test. The error and average error between the experimental and analytical results for each test is displayed in Figures 5.6(a) and 5.6(b). Although, the error becomes less constant as the speed and pressure drop increases, this may just indicate the lack of quantification of a loss that increases with speed. This provides insight into what losses may need to be explored further. The average error of each test creates a linearly increasing

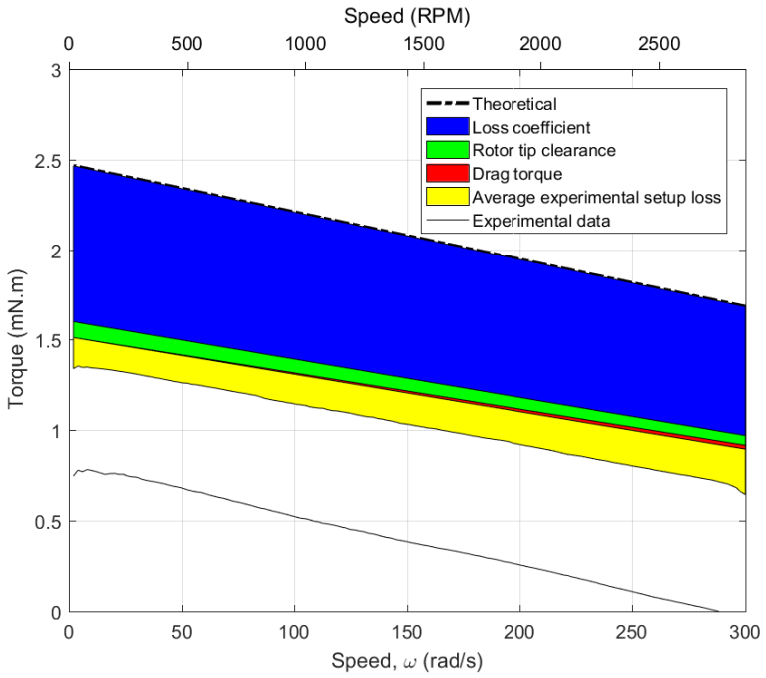


Figure 5.5: Model torque results for a pressure drop of 1.9 psi with identification of losses compared to the experimental torque-speed data.

trend as the pressure drop across the system increases. Increasing losses would be expected at higher pressures and speed, especially viscous or friction losses. However, higher pressure testing could be conducted to verify whether the trend continues in this way as expected. The maximum power and mechanical efficiency was also calculated for each test using the analytical model and was compared to the results of the experiment, as shown in Figure 5.6(c). This plot displays the similarity in trend between the anaytical results and the experimental data, which may suggest the model is performing as intended, yet only shifted from the remaining unidentified error. Although the percent error in the results is approximately 70-80%, the total magnitude for torque error is less than 0.75 mNm for all cases.

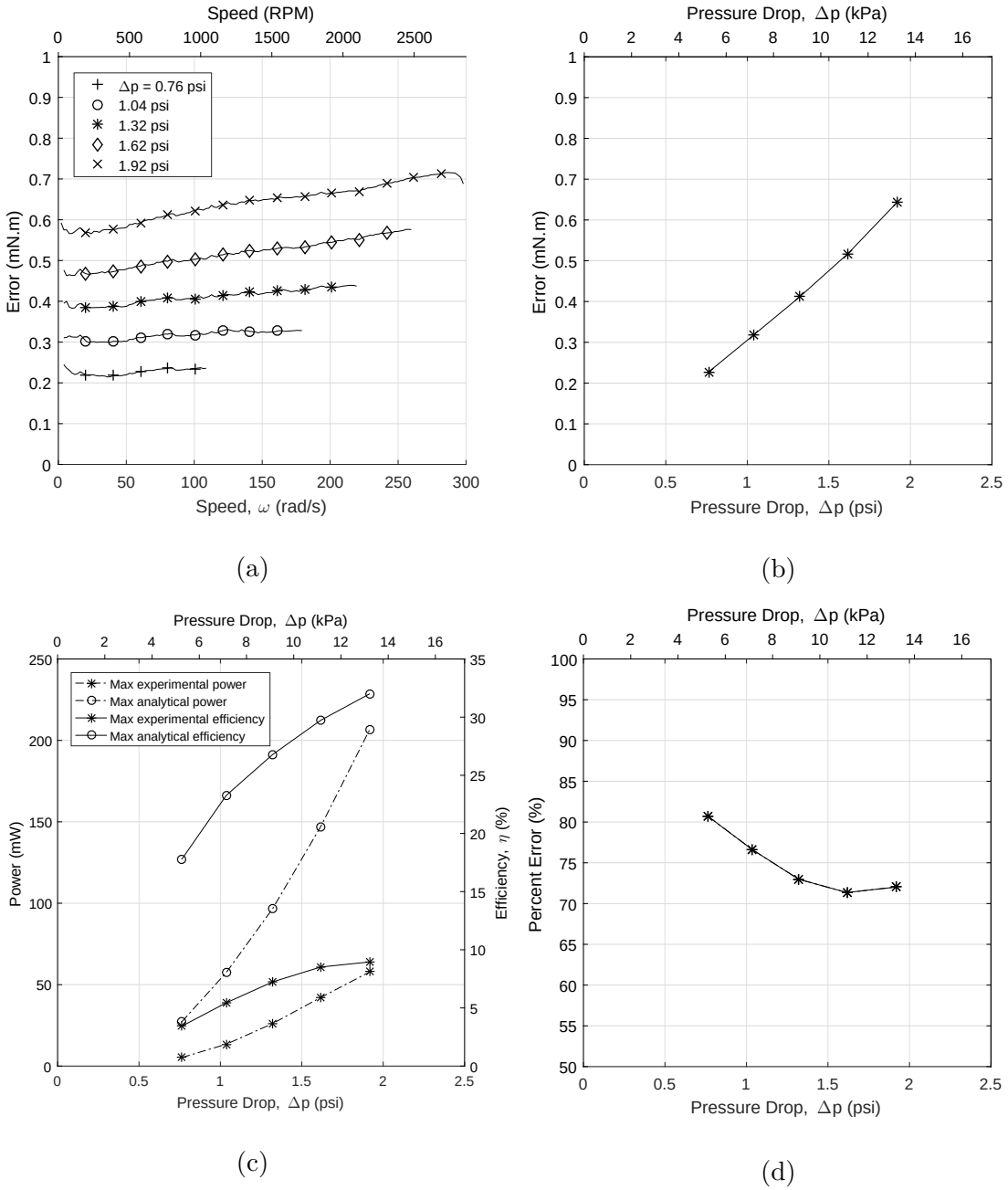


Figure 5.6: (a) Calculated difference between the updated analytical model torque and experimental torque and (b) the mean of each error. (c) The maximum mechanical power and efficiency of each pressure differential test calculated using the analytical model compared to the experimental results and (d) the remaining percent error at the maximums.

The error that is present between the analytical model and the experimental results is significant. However, there are several factors that are predicted to be a contributing source of the remaining loss. For one, there is an uncertainty attached to the experimental setup loss. The model uses the average of three tests, but the actual could be in the higher loss range. Based on the variance of the collected data, there is question as to how accurate it is in representing this loss. This could only be settled with additional testing or improved experimental setup.

Another uncertainty unaccounted for is the physical modeling uncertainty. Although the printing method used to create the prototype is known for its high resolution, the accuracy of the print can vary based on the geometry and build configuration. The accuracy for the method and material used is 0.1 mm. The model is extremely sensitive to geometric properties and 0.1 mm is a significant value compared to the size of the part's key features. It is unlikely that every key dimension is off by this amount in the worst case scenario. However, certain key dimensions such as nozzle exit width could potentially contain this error, which would affect the jet velocity and thereby, overall torque and speed. For reference, this accuracy would affect the width of the nozzle exit, or jet area, by 10% or 5% for length. To verify the prototype dimensions, it would be useful to examine the parts under a microscope in which measurements could be taken of each key feature.

The nozzle exit and the rotor blades, which are both angled or pointed at the ends, could be impacted by the resolution capabilities of the printer as well. Although the resolution capability is high, these features are designed about the smallest capable size. The resolution and accuracy at the blade edges may affect the intended angle of the blades, which is designed to be tangential to the curve of the blade at this

point. This could ultimately affect the angle of incidence. When referring to the angle of incidence, we are referring to the angle between the relative jet velocity and the angle of the rotor blade. At optimum speed, this angle should be equal to zero if the nozzle angle and rotor angles were designed according to the velocity diagram. The angle of incidence or total impact of the jet may also be affected by the spacial dimension between the rotor and stator, as a specific space was accounted for in the design process. The rotor extensions were designed to mitigate inconsistency of this space in the assembly process, yet there is still an amount of leeway.

In order to better understand the sources of error that exist in the current model when compared to the experimental data, computational fluid dynamics (CFD) would best represent the losses experienced by the design. This would help separate losses due to experimental setup and prototype modeling from those inherited by the proposed design and flow configuration. In many studies, analytical modeling is compared with both experimental data and CFD results. While there are uncertainties in this method as well, the visual aspect of this method allows for further exploration of loss sources in a 3D space that were difficult to identify or quantify and provides the opportunity to optimize those locations that result in significant loss for follow-up designs. However, CFD analysis is outside the scope of this work, but may be suggested for future works.

## 5.6 Summary

This chapter discussed in depth the losses and uncertainties identified in the prototype design and displayed how they can be accounted for in the analytical model. The losses included nozzle discharge, viscous flow effects, and abrupt changes in area, all

captured with a flow coefficient. Clearance losses were also identified in both the stator and rotor designs, resulting in a decreased jet velocity and torque, respectively. The drag torque caused by fluid between rotating parts was estimated and found to be minimal. However, drag torque as a result of bearings and shaft coupling was quantified during experimental testing and was presented. Finally, the model updated with the quantified losses was compared to the experimental results showing a major improvement yet still with a remaining error, on the order of 70-80%. This was described as uncertainty losses in geometry and experimental accuracy.

## Chapter 6

# Model Application

The purpose of the analytical model is to provide the capability to predict the performance of the turbine design for a given pressure within a real-world, marine application. The viability of the design can then be assessed for an intended application before final development and integration of the system for use. While applications within the marine environment vary in energy expenditure, size, and travel, the design proposed is intended to be adjustable to meet the needs of each application. However, for this paper alone, the focus is on the integration of the turbine design and pressure energy harvesting method in marine animal tags. Within this chapter, output at a higher pressure and the electrical efficiency is assessed and compared to the current energy source for common telemetry tags.

## 6.1 Increased pressure performance assessment

The goal of the energy harvesting method is to not only match the current energy expenditure of the tags, but also exceed them such that the tags may be able to include

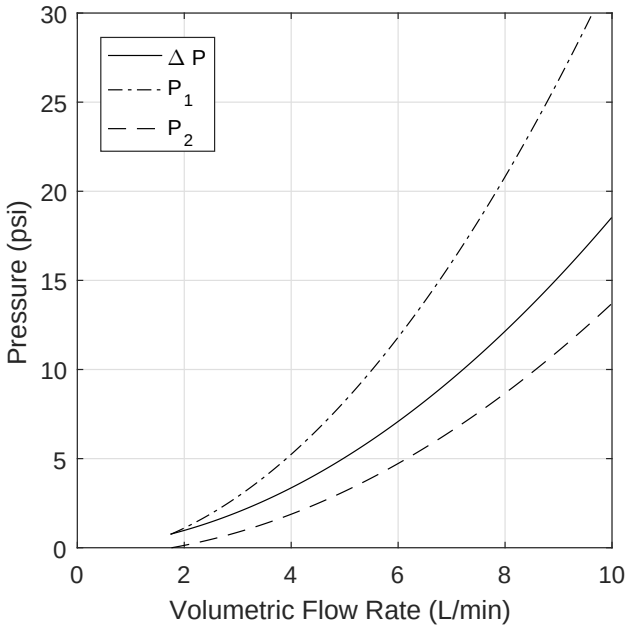


Figure 6.1: Measured input pressure, output pressure, and calculated pressure drop in relation to the measured flow rate.

more sensor capabilities or transmit more data daily. To explore the capabilities of the turbine further and assess whether it is capable of providing sufficient or more than needed power to the tag, an estimate can be made with the model using a higher pressure input. With the uncertainty remaining in the model, an assumption must be made for the higher pressure prediction analysis. Here the assumption will be that the prediction is based on the prototype and experimental setup as-is. This means improvements have not been made to the parts' accuracy, test setup, or assembly. Therefore, the remaining uncertainty loss will be accounted for in this assessment. A linear trendline fit to the average error results in Figure 5.6(b) is used to determine the estimated error for the corresponding pressure drop. The value is subtracted directly from the total torque equation.

The pressure chosen for this analysis is an input pressure of 20 psig, approximately 14 m below the ocean's surface. Considering the model does not only utilize input pressure, we must determine the entire pressure drop across the system, which can be found with the experimental data. Figure 6.1 shows the trend-lines of the measured pressure input, output, and differential pressure in relation to the measured flow rate. At an input pressure of 20 psig, the pressure drop is approximately 11.7 psi and the corresponding flow rate is 7.8 L/min. Recall the flow rate is used to calculate the loss coefficient. However, this could also be estimated with the trend shown in Figure 5.2, as previously discussed. Applying these inputs to the model, we obtain the torque-speed curve, shown in Figure 6.2, followed by the calculated mechanical power output and mechanical efficiency. The stall torque and no-load speed are 6.56 mNm and 1162 rad/s, or 11,096 RPM, respectively. The maximum mechanical power output of the turbine is 1.9 W with an efficiency of approximately 18% at a speed of 580 rad/s, or 5528 RPM. At this point, the nominal torque is 3.28 mNm. With these parameters defined, a motor can be selected to be used as a generator to transfer the mechanical energy into useable electrical energy.

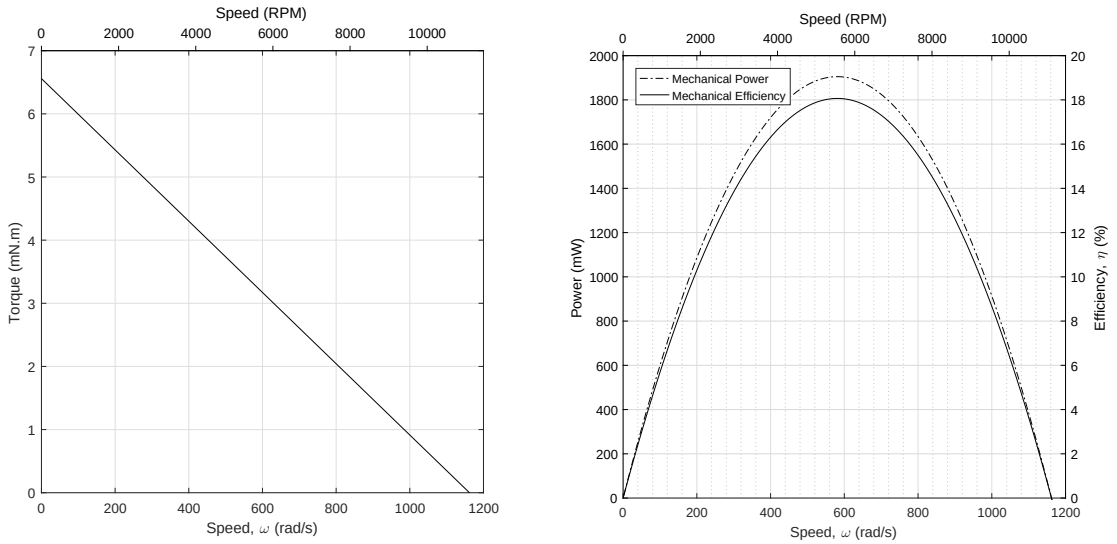


(a) (b)

Figure 6.2: Analytical model results for an input pressure of 20 psi, including (a) torque and (b) mechanical power output and efficiency for a range of speed.

## 6.2 Mechanical to electrical energy transfer

Operation of a motor in reverse provides generator capability by transferring the mechanical power output of the turbine into electrical power. The mathematical relationship used for motor selection is similar when used as a generator, except now torque and speed are inputs and voltage and current are the outputs, and motor losses still apply. With a known mechanical torque input ($M_{in}$), the motor current ($I$) can be calculated using Equation 6.1.

$$I = \frac{M_{in}}{k_M} - I_0 \tag{6.1}$$

where $I_0$ is the no-load current in Amps and $k_M$ is the torque constant in mNm/Amp. The motor output voltage ($V$) can then be calculated using Equation 6.2.

$$V = \frac{n}{k_n} - R_{mot} I \tag{6.2}$$

where $n$ is the speed in RPM, $k_n$ is the speed constant in RPM/Volt, and $R_{mot}$ is the motor resistance in Ohms. The term on the right side of the equation is subtracted from the total output voltage because a portion of the voltage is required to overcome the internal resistance of the winding. Without a complete analysis of how to find the most efficient motor for pairing with a turbine, a basic analysis was done to attempt to match the power curves of the turbine to a motor/generator output. The motor with a nominal torque and speed similar to that of the turbine was selected. Having similar nominal values allows the turbine and motor to operate close to maximum power for each for the given pressure. The motor selected is a 26 mm diameter A-max brushed DC maxon motor (part number 353078) [1]. The desired known values are displayed in Table 6.1.

Table 6.1: Known variables for turbine-motor matching [1].

| Variable | Stator vane |
|---|---|
| $M_{in}$ | 3.28 mNm |
| $n$ | 5528 RPM |
| $I_0$ | 78.9 mA |
| $k_M$ | 5.84 mNm/A |
| $k_n$ | 1640 RPM/V |
| $R_{mot}$ | 0.39 Ω |

At nominal torque and speed, a current of 0.49 A and a voltage of 3.15 V is achieved on the output of the motor/generator. This results in an electrical power output ($P_{el} = VI$) of 1.54 W. The efficiency of the motor/generator ($\eta_g$) can be calculated using Equation 6.3, where $P_{el}$ is divided by $P_{mech}$, the mechanical power

output of the turbine.

$$\eta_g = \frac{P_{el}}{P_{mech}} \tag{6.3}$$

The generator efficiency is 80.96% at this operating point, which is slightly less than the rated motor efficiency of 84%, but is expected to be less. The total efficiency ($\eta_{total}$) of the system can be calculated using Equation 6.4, $\eta_t$ is the turbine efficiency, which we had determined was 18%. Therefore, the total efficiency of the system is approximately 14.6%.

$$\eta_{total} = \eta_g \eta_t \tag{6.4}$$

The electrical power output of the system when compared to the highest energy expenditure of the telemetry tags discussed in this paper, 300 J/day, is more than enough to supplement their current power source. Other marine telemetry tags have reported using as much as 0.5 W per data transmission. Yet, the 1.5 W produced by this system would be sufficient for these tags as well. This suggests the turbine-motor assembly is a viable transduction method for pressure energy harvesting, as an ample amount of power can be produced with a relatively low pressure differential of 11.7 psi.

## 6.3 Application discussion and integration

Although the results of the higher pressure input test, claim an efficiency double that of the previous tests, the uncertainty in the result is larger. For a system of this size, it is difficult to predict how performance will be effected at such high speeds.

This can only be validated through additional testing or CFD analysis. However, this estimate provides insight into the potential power outputs that can be reached. To transfer and store the most energy each day, we may be able to gain small amounts of power in increments as the animal dives and resurfaces. Recall the integration configuration as mentioned at the start of this paper, which includes the turbine as the transduction method between two flexible bladder accumulators. Refer back to the pressure energy harvesting literature review for examples of similar systems.

In summary, as an animal dives, the pressurized sea water at depth compresses a fluid-filled bladder forcing the fluid through the stator and rotor into the bladder of the second accumulator, filled with ambient gas until equillibrium pressure is reached in both accumulators. During the ascent, the sea water is less pressurized than the internal gas, which then pushes back on the fluid-filled bladder to return to a balanced state. Due to the small size of the tag, the accumulators must also be small in volume. With the fluid flow speeds relatively high, the volumes would fill extremely quick provided a high pressure drop across the system, allowing for only one harvesting opportunity during a descent or ascent. In addition to this, the pressure drop would not be consistent as the downstream accumulator fills and the pressure begins to equalize. This may affect the overall efficiency and rated power output optimized for a particular torque and speed and may not charge the batteries adequately. To mitigate this, a bleed valve can be integrated to allow only a certain amount of flow to bleed through over time. The system will consistently attempt to find equillibrium as the accumulator fills though the animal continues to dive deeper, until the accumulator is completely full. This would allow for a more consistent mechanical power input for the rated motor and an extended time period of amperage flowing to the rechargeable

batteries.

## 6.4 Summary

This chapter included a brief assessment of the viability of the turbine design for transduction of pressure energy. The analytical model was used to predict the turbine output power given a higher pressure input. Then a DC motor, used as a generator, was matched theoretically to the mechanical power and used to calculate the transfer of the mechanical input to electrical power output. The output and system efficiency was compared to that of the energy expended by marine telemetry tags and the results showed the design provides adequate supplemental energy compared to the batteries currently used. Lastly, a discussion of how the turbine may be implemented into a marine telemetry tag, not excluding other larger-scaled remote systems, was discussed in depth.

# Chapter 7

# Conclusions

## 7.1 Contributions

The contribution of the work presented in this thesis is the combination and modification of known analysis methods of common turbomachinery and hydropower systems to adequately model a hydrokinetic turbine prototype on the scale of millimeters. The verification of the analytical model through experimental testing provided identification and quantification of losses experienced on this scale. The effects of downsizing on efficiency due to these losses provides information for future exploration and implementation of miniature turbine technology for remote micro-systems. This work also contributed to the novel idea of pressure energy harvesting in the marine environment by assessing the potential energy transferring capabilities with a turbine operating at a given pressure differential.

## 7.2 Future work

In future works, further testing of the turbine may be beneficial for characterization with higher pressures and speeds. Manufacturing of the turbine from metal before further testing may decrease the uncertainty in geometric properties and in return, improve strength and surface finish. Variations to the design could also be made. This includes returning to the longer blades as originally designed, while maintaining the necessary changes made during the evolution of the prototypes. This is predicted to increase the torque and efficiency as well, as clearance losses will be reduced. Stator vane and rotor blade number can be optimized for the desired flow rate, system size, and power output. Lastly, a prototype of the reversible accumulator system can be developed in future works as described in the application discussion previously. The viability of pressure energy harvesting can then be assessed more adequately with a complete system.

## 7.3 Summary

A hydrokinetic turbine on the scale of millimeters was designed, developed, and analyzed using common turbomachinery concepts, such as the velocity diagram for an impulse, axial turbine. An analytical model, derived from Reynold's Transport Theorem, was created to calculate the torque-speed curves, power output, and efficiency of the turbine at various flow rates or pressure drop. Prototypes of the turbine were experimentally tested with a rheometer to validate the analytical model and identify sources of loss in the system. The prototype had undergone various design changes as experience with the equipment, CAD tools, and analytical methods progressed.

Modifications included blade angle, size, and shape.

At approximately 1.92 psi, a maximum mechanical power output of 57.5 mW and a mechanical efficiency of 9% was reached. An increasing trend in maximum power output and efficiency was seen, suggesting that at higher pressures more power and possibly higher efficiencies are obtainable. Through testing, losses such as minor head loss, internal leakage, drag torque, and experimental setup losses were identified and applied to the analytical model for comparison. Losses were found to increase linearly with pressure as expected. The remaining percent error of 70-80% was predicted to be due to physical modeling and experimental setup uncertainties.

The anaytical model and error trends were used to predict the performance of the turbine for a higher pressure input to assess the viability of implementing the transduction method in a system capable of powering small marine telemetry tags. At 14 m below the ocean's surface, the turbine experiencing an input pressure of 20 psig, was predicted to output 1.9 W with a conversion efficiency of 18%. This prediction model was then matched theoretically with a DC brushed motor to be run as a generator, resulting in an electrical power output of 1.54 W with a total conversion efficiency of 14.6%. The results suggested the proposed transduction method is a viable option for powering marine animal tags with integration of a pressure harvesting system. Future works includes further testing of a machined turbine with optimized blade geometry, CFD analysis, and implementation of the accumulator design for harvesting pressure, for not only telemetry tags, but also larger scale systems such as AUVs and ROVs.

# Bibliography


[1] maxon motor, *Online Shop*, 2018 (accessed April 15, 2018). `https://www.maxonmotorusa.com/maxon/view/catalog/`.

[2] T. Stephens, "Elephant seal tracking reveals hidden lives of deep-diving animals." electronic, 2012.

[3] M. W. Shafer, G. Hahn, and E. Morgan, "A hydrostatic pressure-cycle energy harvester," in *SPIE Smart Structures and Materials+ Nondestructive Evaluation and Health Monitoring*, pp. 94310F–94310F, International Society for Optics and Photonics, 2015.

[4] Wildlife Computers, *SPLASH10: Backmount Suite Specifications*, 2014.

[5] The Costa Lab, *Northern Elephant Seal GPS and Depth Data*. The Costa Lab, March 2014. GPS and Depth Data.

[6] F. Wang, L. Gu, and Y. Chen, "An energy conversion system based on deep-sea pressure," *Ocean Engineering*, vol. 35, no. 1, pp. 53–62, 2008.

[7] SGM Machinery, *GRW: Quantum leap in dental technology*, 2018 (accessed April 15, 2018). `http://www.sgm-machinery.com/news_detail.asp?id=385`.

[8] G. C. Hays, C. J. A. Bradshaw, M. C. James, P. Lovell, and D. W. Sims, "Why do argos satellite tags deployed on marine animals stop transmitting?," *Journal of Experimental Biology*, vol. 349, pp. 52–60, 2007.

[9] P. Ryan, S. Petersen, G. Peters, and D. Grémillet, "Gps tracking a marine predator: the effects of precision, resolution and sampling rate on foraging tracks of african penguins," *Marine Biology*, vol. 145, no. 2, pp. 215–223, 2004.

[10] S. M. Tomkiewicz, M. R. Fuller, J. G. Kie, and K. K. Bates, "Global positioning system and associated technologies in animal behaviour and ecological research," *Philos. T. Roy. Soc. B*, vol. 365, pp. 2163–2176, 2010.

[11] A. Harb, "Energy harvesting: State-of-the-art," *Renewable Energy*, vol. 36, no. 10, pp. 2641–2654, 2011.

[12] J. Donelan, Q. Li, V. Naing, J. Hoffer, D. Weber, and A. Kuo, "Biomechanical energy harvesting: generating electricity during walking with minimal user effort," *Science*, vol. 319, no. 5864, pp. 807–810, 2008.

[13] H. P. Tan, P. W. Q. Lee, W. K. G. Seah, and Z. A. Eu, "Impact of power control in wireless sensor networks powered by ambient energy harvesting (wsn-heap) for railroad health monitoring," in *2009 International Conference on Advanced Information Networking and Applications Workshops*, pp. 804–809, May 2009.

[14] M. W. Shafer, R. MacCurdy, D. W. Winkler, C. G. Guglielmo, and E. Garcia, "The case for energy harvesting on wildlife in flight," *Smart Mater. Struct.*, vol. 24, p. 025031, January 2015.

[15] R. MacCurdy, T. Reissman, E. Garcia, and D. Winkler, "A methodology for applying energy harvesting to extend wildlife tag lifetime," in *Proc. ASME 2008 Conf. Smart Mater. Adap. Struct. Intel. Syst.*, no. 48692, pp. 121–130, ASME, 2008.

[16] D. P. Costa, B. Block, S. Bograd, M. A. Fedak, and J. S. Gunn, "Topp as a marine life observatory: Using electronic tags to monitor the movements, behaviour and habitats of marine vertebrates," *Proceedings of OceanObs*, vol. 9, pp. 21–25, 2010.

[17] Wildlife Computers, *SPOT5: Backmount Suite Specifications*, 2014.

[18] Wildlife Computers, *SPOT5: Finmount Suite Specifications*, 2014.

[19] K. Ng. Wildlife Computers Engineer, Personal Communication, January 2014.

[20] Wildlife Computers, *SPLASH10: Finmount Suite Specifications*, 2014.

[21] D. Costa. Personal Communication, January 28 2016.

[22] J. M. Gilbert and F. Balouchi, "Comparison of energy harvesting systems for wireless sensor networks," *International Journal of Automation and Computing*, vol. 5, pp. 334–347, Oct 2008.

[23] E. E. Aktakka, H. Kim, and K. Najafi, "Energy scavenging from insect flight," *J. Micromech. Microeng.*, vol. 21, no. 095016, 2011.

[24] Desert Star Systems, *SeaTag-3D*, 2015 (accessed January 15, 2016). `http://desertstar.com/product/seatag-geo/`.

[25] Telemetry Solutions, *Solar power intensifies GPS data sets*, 2017 (accessed June 1, 2017). `http://www.telemetrysolutions.com/solar-power.php`.

[26] Microwave Telemetry Inc., *Solar PTT Price List*, 2015 (accessed July 7, 2015). `http://www.microwavetelemetry.com/bird/prices.cfm`.

[27] M. D. Ageev, D. R. Blidberg, J. Jalbert, C. J. Melchin, and D. P. Troop, "Results of the evaluation and testing of the solar powered auv and its subsystems," in *Autonomous Underwater Vehicles, 2002. Proceedings of the 2002 Workshop on*, pp. 137–145, IEEE, 2002.

[28] D. C. Webb, P. J. Simonetti, and C. P. Jones, "Slocum: an underwater glider propelled by environmental energy," *IEEE Journal of Oceanic Engineering*, vol. 26, pp. 447–452, Oct 2001.

[29] J. Nicholson and A. Healey, "The present state of autonomous underwater vehicle (auv) applications and technologies," *Marine Technology Society Journal*, vol. 42, no. 1, pp. 44–51, 2008.

[30] G. W. Boehlert, D. P. Costa, D. E. Crocker, P. Green, T. O'Brien, S. Levitus, and B. J. Le Boeuf, "Autonomous pinniped environmental samplers: using instrumented animals as oceanographic data collectors," *Journal of Atmospheric and Oceanic Technology*, vol. 18, no. 11, pp. 1882–1893, 2001.

[31] M. W. Shafer and E. Morgan, "Energy harvesting for marine-wildlife monitoring," in *Proc. ASME 2014 Conf. Smart Mater. Adap. Struct. Intel. Syst.*, no. 7630, ASME, Sept. 8-10, Newport, RI 2014.

[32] J. Dyson and B. Darvell, "Flow and free running speed characterization of dental air turbine handpieces," *Journal of dentistry*, vol. 27, no. 7, pp. 465–477, 1999.

[33] J. Dyson and B. Darvell, "Torque, power and efficiency characterization of dental air turbine handpieces," *Journal of dentistry*, vol. 27, no. 8, pp. 573–586, 1999.

[34] A. H. Epstein, "Millimeter-scale, micro-electro-mechanical systems gas turbine engines," *Transactions of the ASME-A-Engineering for Gas Turbines and Power*, vol. 126, no. 2, pp. 205–226, 2004.

[35] L. Fu, Z. Feng, and G. Li, "Experimental investigation on overall performance of a millimeter-scale radial turbine for micro gas turbine," *Energy*, 2017.

[36] J. Peirs, D. Reynaerts, and F. Verplaetsen, "A microturbine for electric power generation," *Sensors and Actuators A: Physical*, vol. 113, no. 1, pp. 86–93, 2004.

[37] T. Wright, *Fluid Machinery: Performance, Analysis, and Design*. Taylor & Francis, 1999.

[38] P. Pritchard, *Fox and McDonald's Introduction to Fluid Mechanics*. John Wiley & Sons, 2011.